

Lawrence Berkeley National Laboratory

LBL Publications

Title

High Reynolds Number Simulations of Axisymmetric Tornado-Like Vortices with Adaptive Mesh Refinement

Permalink

<https://escholarship.org/uc/item/2d604027>

Authors

Nolan, David S

Almgren, Ann S

Bell, John B

Publication Date

1999-07-01

Copyright Information

This work is made available under the terms of a Creative Commons Attribution License, available at <https://creativecommons.org/licenses/by/4.0/>



ERNEST ORLANDO LAWRENCE BERKELEY NATIONAL LABORATORY

High Reynolds Number Simulations of Axisymmetric Tornado-Like Vortices with Adaptive Mesh Refinement

David S. Nolan, Ann S. Almgren, and John B. Bell

Computing Sciences Directorate
Mathematics Department

July 1999

Submitted to

Journal of the Atmospheric Sciences



REFERENCE COPY |
Does Not |
Circulate |
Bldg. 50 Library - Ref.
Lawrence Berkeley National Laboratory

DISCLAIMER

This document was prepared as an account of work sponsored by the United States Government. While this document is believed to contain correct information, neither the United States Government nor any agency thereof, nor the Regents of the University of California, nor any of their employees, makes any warranty, express or implied, or assumes any legal responsibility for the accuracy, completeness, or usefulness of any information, apparatus, product, or process disclosed, or represents that its use would not infringe privately owned rights. Reference herein to any specific commercial product, process, or service by its trade name, trademark, manufacturer, or otherwise, does not necessarily constitute or imply its endorsement, recommendation, or favoring by the United States Government or any agency thereof, or the Regents of the University of California. The views and opinions of authors expressed herein do not necessarily state or reflect those of the United States Government or any agency thereof or the Regents of the University of California.

**High Reynolds Number Simulations of Axisymmetric
Tornado-Like Vortices with Adaptive Mesh Refinement**

David S. Nolan,*

Department of Atmospheric Science
Colorado State University
Fort Collins, Colorado

Ann S. Almgren and John B. Bell

Computing Sciences Directorate
Mathematics Department
Ernest Orlando Lawrence Berkeley National Laboratory
University of California
Berkeley, California 94720

July 1999

*Corresponding author address: Dr. David S. Nolan, Department of Atmospheric Science,
Colorado State University, Fort Collins, CO 80523; nolan@chandra.atmos.colostate.edu

This work was supported in part by the Office of Science, Office of Advanced Computing Research,
Mathematical, Information, and Computational Sciences Division, Applied Mathematical Sciences
Subprogram, of the U.S. Department of Energy under Contract No. DE-AC03-76SF00098, and the Office of
Naval Research under Contract N00014-93-1-0456 P0006.

Abstract

Axisymmetric numerical simulations continue to provide new insight into how the structure, dynamics, and maximum windspeeds of tornadoes, and other convectively-maintained vortices, are influenced by the surrounding environment. This work is continued with a new numerical model of axisymmetric incompressible flow that incorporates adaptive mesh refinement. The model dynamically increases or decreases the resolution in regions of interest as determined by a specified refinement criterion. Here, the criterion used is based on the cell Reynolds number, so that the flow is guaranteed to be laminar on the scale of the local grid spacing.

The power of adaptive mesh refinement is used to investigate the effects of the size of the domain, the location and geometry of the convective forcing, and the effective Reynolds number (based on the choice of the eddy viscosity ν) on the behavior of the vortex. In particular, the claim that the vortex Reynolds number Γ/ν , which is the ratio of the far-field circulation to the eddy viscosity, is the most important parameter for determining vortex structure and behavior is found to be valid over a wide variety of domain and forcing geometries. Furthermore, it is found that the vertical scale of the convective forcing only affects the vortex inasmuch as this vertical scale contributes to the total strength of the convective forcing. The horizontal scale of the convective forcing, however, is found to be the fundamental length scale in the problem, in that it can determine both the circulation of the fluid that is drawn into the vortex core, and also influences the depth of the swirling boundary layer. Higher mean windspeeds are sustained as the eddy viscosity is decreased; however, it is observed that the highest windspeeds are found in the high-swirl, two-celled vortex regime rather than in the low-swirl, one-celled regime, which is opposite to

what had been previously observed.

The conclusions drawn from these results are applied to dimensional simulations with scales similar to the tornado environment and with a more realistic rotating environment. Tornado-like vortices are reproduced, using a constant eddy viscosity with such values as $20 \text{ m}^2\text{s}^{-1}$, which have radii of maximum winds and boundary layer depths which are very similar to those recently observed with portable Doppler radar.

1. Recent results on the structure and dynamics of tornado-like vortices

Axisymmetric modelling of the forced convergence of rotating fluid near a lower boundary has been a valuable tool in the study of a tornado's interaction with the surface. The early models, such as Rotunno (1977,1979), Walko and Gall (1986), and Howells et. al. (1988) were designed to represent axisymmetric versions of laboratory models such as those used by Ward (1972) and Church et. al. (1979). In these models (physical and numerical) rotating air was fed into the lower levels of a cylindrical chamber and drawn out through the top with some kind of forcing (a fan or boundary conditions). The most important result from the laboratory studies was that the structure and behavior of the resulting vortex was well-correlated with the ratio of the circulation of the fluid entering the vortex chamber to the volume flow rate of the air through the chamber, a parameter generally known as the swirl ratio. Perhaps the most important discovery found with the numerical models, first made by Rotunno (1979) and furthered explored by Howells et. al. (1988), is that the near-surface windspeeds are substantially higher when no-slip boundary conditions are used at the surface. This observation identifies the importance of radial inflow in the swirling boundary layer which amplifies the convergence of the rotating fluid just above the boundary layer.

Rather than using a domain based on laboratory models, Fiedler (1993, 1994) (hereafter F93 and F94) simulated the formation of a vortex in a closed domain through the convergence of incompressible fluid in solid body rotation. This convergence was forced by the imposition of a

fixed buoyancy function along the center axis. The integral of this vertical forcing along the center axis provides a velocity scale that can be considered analogous to the same velocity scale associated with the convective available potential energy (CAPE) in the atmosphere. This velocity scale provides a direct connection between the maximum windspeeds in a tornado and those observed in the closed-domain model.

Nolan and Farrell (1999a) (hereafter NF99) used a similar numerical model of axisymmetric, incompressible fluid flow in a closed domain to study tornado-like vortices. Rather than focusing on the maximum windspeeds, they examined how the structure and dynamics of such vortices depend on the parameters that arise from dimensional analysis. They found that the results were best described by two dimensionless parameters. One of these is a *convective* Reynolds number

$$Re_C = \frac{UL}{\nu}, \quad (1.1)$$

where U , defined by

$$\frac{U^2}{2} = \int_0^{Z_{max}} F_z(0, z) dz, \quad (1.2)$$

is a velocity scale based on the integral of the convective forcing [see (3.1) below] along the center axis of the domain, L is the length scale in the domain, and ν is the model eddy viscosity. The other dimensionless parameter is a *vortex* Reynolds number

$$Re_V = \frac{\Gamma}{\nu} \quad (1.3)$$

where Ω is the rotation rate of the fluid and $\Gamma = \Omega L^2$ is the circulation of the fluid in the far field.

The way in which these parameters controlled the results could be measured both in terms of the maximum azimuthal windspeeds in the vortex core and in terms of the structure and time-dependen-

dent behavior of the flow. For example, the average maximum windspeeds were found to follow the relation:

$$V_{max} = C_v U \quad (1.4)$$

where U is the convective velocity scale from (1.2) and C_v is a velocity coefficient whose value typically lies between 0.6 and 0.8 and depends, albeit weakly, on both Re_V and Re_C . Furthermore, NF99 found that there is a particular choice of Re_V which maximizes C_v for all values of Re_C , and this maximum value of C_v increases with increasing Re_C . The physical interpretation of these relationships is that there is a universal structure for the tornado-like vortex which maximizes the azimuthal windspeeds. The windspeeds will increase as the viscosity is decreased, provided the circulation in the far-field is adjusted so as to maintain the ideal structure.

The value of C_v is significant because one of the problems with earlier axisymmetric simulations is that they did not predict sufficiently high windspeeds. For example, with a CAPE of 2500 J kg^{-1} we have a convective velocity scale of $U=64 \text{ m s}^{-1}$; for a typical value of $C_v=0.7$ we would have only $V_{max}=44 \text{ ms}^{-1}$. Values of C_v closer to 1.0 would bring the model results closer to typically observed or estimated tornadic windspeeds of $70\text{-}80 \text{ m s}^{-1}$. By using a spatially varying viscosity, so that the upper levels of the domain did not require high resolution, Fiedler (1994) did observe azimuthal windspeeds which indicate $C_v \approx 1.1$ when the nondimensional viscosity in the boundary layer was $\nu=0.000125$, one quarter of the value used for most of the simulations in F93 and NF99. However, more recently reported axisymmetric simulations with similar configurations by Fiedler (1998) indicate that the long-time mean of C_v in those cases is close to 1.0.

Remarkably, the structure of the flow through the vortex core, and whether this flow is steady or unsteady, was found by NF99 to depend strongly on the vortex Reynolds number Re_V and only very weakly on Re_C . While the laboratory modellers (Ward, 1972; Church et al., 1979)

found that the structure of the vortex could be predicted by the swirl ratio, in a closed-domain model the low-level inflow of radial and angular momentum are not under the control of the modeller, but rather are determined by the circulation throughout the entire domain. NF99 introduced an *internal* swirl ratio which is analogous to the swirl ratio for laboratory experiments except that it is appropriate for closed-domain numerical models of tornado-like vortices. This internal swirl ratio is defined using an arbitrary control volume around the intense part of the vortex to measure the ratio of the circulation entering the vortex core to the volume flow rate through the core, i.e.:

$$S_I = \frac{r_0 \int_0^{h_0} \Gamma^*(r_0, z) dz}{2h_0 \int_0^{r_0} w(r, z_0) 2\pi r dr} \quad (1.5)$$

where $\Gamma^*(r, z) = 2\pi r v(r, z)$ is the circulation¹, v and w are the azimuthal and vertical velocity fields, and r_0 and h_0 are the radius and height of the control volume that is adjacent to the surface and surrounds the vortex core. Despite the $r_0/2h_0$ prefactor held over from the original swirl ratio, observed numerical values of S_I are not similar to those of the original swirl ratio; furthermore S_I is arbitrary since it depends strongly on the choice of control volume (r_0 and h_0). However, NF99 found that this definition of swirl ratio shares the same utility as its predecessor in that a correlation can be made between the structure of the tornado-like vortex and the value of S_I , such that as S_I increases the vortex transitions from a one-celled vortex to a drowned vortex jump and ultimately to a two-celled vortex. As shown in Fig. 1, it was found that the value of S_I was approximately a function of only Ω/v for a wide range of parameter space, thus showing how the structure of the flow in the vortex core is a function of Re_V but not of Re_C [when the length scale

1. A factor of 2π is included in the circulation which appears in the swirl ratio. Elsewhere it is neglected.

is fixed, $\Gamma \propto \Omega$]. The unsteadiness of the flow in the core, as measured by the variance of S_I (not shown - see NF99), was nearly zero for $Re_V < 250$, but then rapidly increased for $Re_V > 250$. As can be seen from the lower-right hand part of Fig. 1, the accuracy of the relationship $S_I = f(Re_V)$ appears to break down in this region. This unsteadiness was shown to be caused by axisymmetric disturbances propagating down into the vortex from the upper part of the domain; such downward propagation is allowed to occur by both a decrease in the vertical velocities and an increase in the gradients of the azimuthal winds in the vortex core.

Despite its utility, the internal swirl ratio does suffer from some flaws. First, its definition is quite arbitrary and its value depends strongly on the size and shape of the control volume. Second, we have observed in highly unsteady simulations (usually associated with a two-celled vortex) that occasionally there can be a net flow reversal in the vortex core, such that the internal swirl ratio becomes negative or undefined. An alternative measure of the structure of the vortex is the *vortex aspect ratio*, defined as the ratio of the radius of maximum azimuthal winds (RMW) to the altitude of maximum azimuthal winds (ZMW):

$$A_V = \frac{\text{RMW}}{\text{ZMW}}. \quad (1.6)$$

Fig. 2 shows the mean value of A_V as a function of Ω and v for the same ensemble of simulations as those used to produce Fig. 1. While A_V is not as well matched with Ω/v as is S_I , we can still see a meaningful correlation. It is interesting to note that the correlation is the strongest for large Re_V , which is exactly where S_I has the worst correlation, indicating that the vortex aspect ratio is a more reliable measure of the vortex structure in the unsteady flow regime. Furthermore, the vortex aspect ratio does not become undefined during flow reversals, and unlike the swirl ratio it can be measured directly with Doppler radar [see, for example, the observations of Wurman et al., (1996)

where the location of the maximum azimuthal winds is easily identified].

Working independently and using a fully three-dimensional model with a one-and-a-half order turbulence closure scheme, Lewellen et. al. (1999) also found that the structure of the vortex is well-predicted by a swirl ratio defined on a smaller scale around the vortex core. They also found that this swirl ratio and the associated vortex structure could be modified substantially by varying the angular momentum of the fluid near the surface. This is consistent with NF99 since in that model one of the most important effects of increasing the viscosity is to decrease the angular momentum in the boundary layer.

In this report we further explore the relationships found by NF99 by investigating the dynamics of axisymmetric tornado-like vortices over a wider range of parameters. We also investigate how the geometries of both the model domain and the vertical forcing field affect the results. Section 2 describes the numerical model which uses adaptive mesh refinement so that high Reynolds number simulations in large domains can be performed efficiently. In section 3 the model results are compared to equivalent full-resolution simulations. In section 4 we investigate how the size of the domain, the location of the forcing field, and its geometry affect the vortex dynamics. In section 5 we show the results of simulations with higher Reynolds numbers. Section 6 presents the results of simulations with dimensional scales chosen to reproduce tornado-like vortices with similar length scales as those observed in the atmosphere. In Section 7 we discuss what determines these length scales in the vortex core. Conclusions are drawn in section 8.

2. A Numerical Model for Incompressible, Axisymmetric Fluid Flow with Adaptive Mesh Refinement

a. Equations of motion

We proceed directly to the non-dimensional equations of motion. For a discussion of the

dimensional equations, non-dimensionalization, and the relevance of the dimensionless parameters, see NF99 and earlier references [e.g., Fielder (1993), Howells et. al., (1988)]. For axisymmetric, incompressible flow, the momentum equations in the radial, azimuthal, and vertical directions are, respectively,

$$\frac{\partial u}{\partial t} + u \frac{\partial u}{\partial r} + w \frac{\partial u}{\partial z} - \frac{v^2}{r} = -\frac{\partial p}{\partial r} + \nu \left[\frac{\partial}{\partial r} \left(\frac{1}{r} \frac{\partial}{\partial r} (ru) \right) + \frac{\partial^2 u}{\partial z^2} \right], \quad (2.1)$$

$$\frac{\partial v}{\partial t} + u \frac{\partial v}{\partial r} + w \frac{\partial v}{\partial z} + \frac{uv}{r} = \nu \left[\frac{\partial}{\partial r} \left(\frac{1}{r} \frac{\partial}{\partial r} (rv) \right) + \frac{\partial^2 v}{\partial z^2} \right], \quad (2.2)$$

$$\frac{\partial w}{\partial t} + u \frac{\partial w}{\partial r} + w \frac{\partial w}{\partial z} = -\frac{\partial p}{\partial z} + \nu \left[\frac{1}{r} \frac{\partial}{\partial r} \left(r \frac{\partial w}{\partial r} \right) + \frac{\partial^2 w}{\partial z^2} \right] + F_z, \quad (2.3)$$

while the incompressibility condition is

$$\frac{1}{r} \frac{\partial}{\partial r} (ru) + \frac{\partial w}{\partial z} = 0, \quad (2.4)$$

where u is the radial velocity, v is the azimuthal (swirling) velocity, w is the vertical velocity, p is the pressure, ν is the kinematic viscosity, and F_z is a spatially varying vertical forcing which will be defined later.

b. Numerical integration of the Navier-Stokes equations with AMR

The velocities and pressure in the equations (2.1)-(2.4) are solved using an approximate projection method on an adaptive hierarchy of rectangular grids. The exact details of the method and some examples of its application are described in Almgren, et. al. (1998). In the following sections we will only outline the basic features of the model and its properties; those interested in further understanding of the model should consult Almgren et. al. (1998) and the other references listed below.

(1) The single grid algorithm

In our discretization, the velocity fields are located at cell centers at integer time levels, while the pressure field is defined at nodes (cell corners) at half-time levels. The fundamental method for advancing the radial and vertical velocities and updating the pressure is a fractional step scheme using an approximate projection method. In the first step, an intermediate velocity field is constructed which does not satisfy the incompressibility constraint. In the second step, the incompressibility condition is imposed on the velocity field via the solution of an elliptic equation for the pressure update, resulting in new velocity and pressure fields.

For the nonlinear advection terms, we use a Godunov upwind scheme as described by Almgren et. al. (1996). The velocity field is extrapolated in space and time to define second-order accurate velocities on cell edges one half time step into the future. The incompressibility condition is enforced on the half-step velocities using an approximate projection method. These velocities are then used to compute fluxes which are then differenced to predict the velocity changes at cell centers. The viscous terms are centered in time using a Crank-Nicholson discretization, which requires a parabolic solve for each velocity component.

The details of the approximate projection method are given in Almgren et. al. (1996) and Almgren et. al. (1998). A finite element derivation is used to define stencils for the discrete divergence (D), gradient (G), Laplacian (L) operators. Unlike exact projections, where L is identically DG , in an approximate projection L is a second-order accurate approximation to DG . As a result, the divergence of the resulting velocity field is not exactly zero, but $O(h^2)$ where h is the grid spacing. The advantage of the approximate projection method is that L may be chosen to define an elliptic system which can be solved with standard iterative techniques, and without the local grid decoupling that tends to accompany exact projection operators. The issues surrounding the choice

of exact vs. approximate projections are discussed further in Almgren et. al. (1996) and Almgren et. al. (1999).

The projection operator acts only on the radial and vertical velocities. The evolution of the azimuthal velocity is described by an advection-diffusion equation with an additional source term from conservation of angular momentum. The azimuthal velocity modifies the flow through the centripetal force term, which appears in the radial momentum equation.

(2) Adaptive projection algorithm

We now describe how the single grid algorithm is extended to a hierarchy of nested rectangular grids. The grid hierarchy is composed of different levels ranging from the base grid ($l=0$) to the finest grid ($l=l_{max}$). Each level is represented as a collection of rectangular grid patches of a given resolution. In calculations reported here, the refinement ratio is always 2 in both coordinate directions, such that $\Delta r^{l+1} = \frac{1}{2}\Delta r^l$ and $\Delta z^{l+1} = \frac{1}{2}\Delta z^l$. The grids are properly nested, which means that all the grids of some level $l+1$ lie entirely within the grids of level l . Furthermore, the containment is strict in the sense that, except at physical boundaries, the level l grids are large enough to guarantee that there is a border at least one level l cell wide surrounding each level $l+1$ grid. (Grids at all levels are allowed to extend to the physical boundaries so the proper nesting is not strict there; in this sense $r=0$ is considered a physical boundary.)

The initial creation of the grid hierarchy, and the subsequent regridding operations, are based on refinement criteria specified by the user. In all the calculations presented here, we use as a refinement criterion the *cell Reynolds number*

$$Re_{cell} = \frac{\max\{\Delta r, \Delta z\} \times \max\{\Delta u, \Delta v, \Delta w\}}{\nu}, \quad (2.5)$$

which is the product of the maximum grid spacing and the maximum velocity difference across each cell divided by the kinematic viscosity. We also impose an additional requirement that the

maximum vertical velocity, inward radial velocity, and azimuthal velocity must be resolved at the finest of the current levels. This prevents spurious changes in the maximum velocities, which can occur if the resolution changes at the locations of these maxima. Given grids at level l , we tag cells where the refinement criteria are met (e.g., $Re_{cell} > 10$). The tagged cells are grouped into rectangular patches which are then refined to form the grids at the next level. The process is repeated until either the refinement criterion is satisfied everywhere or a specified maximum level is reached. As the solution advances in time, the regridding algorithm is called every 2 level l time steps to redefine grids at levels $l+1$ through l_{max} . When new grids are created on level $l+1$, the data on these new grids are copied from the previous grids at level $l+1$ if possible; otherwise the data are interpolated from the underlying level l grids.

The adaptive time-step algorithm is perhaps most easily thought of as a recursive procedure, in which to advance some level l , the following steps are taken:

- Advance level l in time as if it were the only level. Supply boundary conditions for the velocity and pressure fields from level $l-1$ (if $l > 0$), and from the physical domain boundaries.
- If $l < l_{max}$, then
 1. Advance level $(l+1)$ 2 times with time step $\Delta t^{l+1} = \frac{1}{2}\Delta t^l$. Use boundary conditions for the velocity and pressure from level l , and from the physical domain boundaries.
 2. Synchronize the data between levels l and $l+1$, and interpolate corrections to higher levels if $l+1 < l_{max}$.

The synchronization step is necessary to correct for the mismatches that occur as a result of the sequential time-stepping of the levels. The nature of the synchronizations depends on the nature of the operation that created the mismatch. For example, the mismatch in advective fluxes between the coarse and fine grids is easily corrected by an explicit refluxing operation, which adds the amount of the mismatch to the coarse cells immediately surrounding the fine grid. The viola-

tion of the elliptic matching conditions at the coarse-fine interface, resulting from the fact that we performed single level rather than composite (i.e., multilevel) solves for the pressure updates, is corrected by a multi-level elliptic solve for a correction to the global pressure field.

This method has been shown to be second-order accurate in space and time (Almgren, et. al., 1998). Due to careful treatment at the coarse-fine interface, analytically conserved quantities are discretely conserved numerically. Also, the method has a free-stream preservation property which guarantees that constant scalar fields remain constant, independent of the behavior of the velocity fields, so that spurious maxima and minima are not generated in the flow.

3. Reproduction of Full-Resolution Results with Adaptive-Mesh Refinement

In this section we use a single-grid version of the model described above to perform a numerical simulation of a tornado-like vortex. We then perform identical simulations with a base grid of substantially lower resolution but which use the adaptive mesh refinement capability of our model. The results will be compared and their differences discussed.

a. The basic simulation and measured parameters of the flow in the vortex core

For purposes of comparison, we will return to the original initial and boundary conditions for Fiedler's (1993) axisymmetric incompressible simulations in a closed domain. The axisymmetric domain lies in the range $0 \leq r \leq 2$ and $0 \leq z \leq 1$, with no-slip, solid-wall boundary conditions on all sides except on the center axis $r=0$. While Fiedler (1993) put his domain into solid-body rotation by incorporating a Coriolis term into the equations of motion, in our case this effect is reproduced by initializing the fluid in solid-body rotation at the same rate $\Omega = 0.2$, and keeping the boundaries fixed at this rotation rate. The flow is driven by a fixed vertical forcing field in the form of a Gaussian bubble in the center of the domain:

$$F_z(r, z) = 1.264e^{-20[r^2 + (z-0.5)^2]} \quad (3.1)$$

In subsequent sections we will vary the location and shape of the convective forcing, so it is useful to rewrite (3.1) as

$$F_z = C_b e^{-\left\{ \frac{r^2}{\sigma_h^2} + \frac{(z-z_{forc})^2}{\sigma_v^2} \right\}} \quad (3.2)$$

where $C_b = 1.264$, $z_{forc} = 0.5$, and $\sigma_h = \sigma_v = 0.2236$ are the horizontal and vertical length scales, respectively.

At $t=0$, the flow is at rest except for the solid-body rotation, i.e., $u = w = 0$ and $v = \Omega r$. The development of a tornado-like vortex from fluid in solid-body rotation has been discussed extensively by Fiedler (1993, 1994) and NF99, so we will not provide a discussion of the development of the vortex, but instead address how well the AMR model reproduces the results with full resolution. For this purpose we ran three simulations of the F93 type: one with a fixed resolution of 256x128 gridpoints in the horizontal and vertical directions, respectively; and two with a base resolution of 64x32 gridpoints and a maximum of two levels of factor two refinement, so that the highest resolution in the regions of dynamical interest matched that of the fixed 256x128 case. The two AMR simulations of the F93 experiment were different only in regards to their refinement conditions: one used as a refinement condition that the cell Reynolds number Re_{cell} [defined above in (2.5)] be less than 20 everywhere, whereas the other required $Re_{cell} < 10$.

Fig. 3 shows the maximum vertical, azimuthal, and negative horizontal velocities in the three F93 simulations from $t=0$ to $t=70$. It is readily apparent that both AMR simulations do a fairly good job of reproducing the full grid results. One can also see that the $Re_{cell} < 10$ simulation is consistently closer to the full grid results than the $Re_{cell} < 20$ simulation. This is demonstrated

even more clearly in Fig. 4, which shows closeups of the maximum vertical and azimuthal velocities separately. While the $Re_{cell} < 20$ simulation occasionally shows significant departures from the full grid solutions, the $Re_{cell} < 10$ simulation follows the full grid solution very closely with occasional deviations on the order of 5% for the vertical velocities and even smaller for the azimuthal and radial velocities.

The AMR code with a properly chosen refinement condition (usually $Re_{cell} < 10$ or less) quite accurately reproduces the results of a full grid simulation for short times. However, over the course of studying a wide variety of refinement conditions for long-time simulations we have found that the AMR code cannot reproduce the exact details of a full grid simulation for long times. As an example, consider the results shown in Fig. 5, which compares the azimuthal and vertical velocity fields at $t=100$ for the AMR simulation and the full-resolution simulation. The results are very similar, in fact nearly indistinguishable for the azimuthal velocities in the vortex core, whereas in the far field, where the resolution of the AMR simulation is lower than that of the full-resolution simulation, one can clearly see some differences. Fig. 6 shows the long-term evolution for each simulation in terms of the maximum windspeeds and the vortex aspect ratio. From these figures we can draw two conclusions: 1) after a period of nearly steady flow in the vortex core, the flow in the core becomes unsteady with large oscillations in the vertical windspeeds and the vortex structure; 2) while the AMR simulation does not follow the evolution of the full resolution simulation exactly, it reproduces the behavior in a statistical sense. Mean values for C_v , the depth of the boundary layer, A_V , and the standard deviation of A_V , are shown in Table 2 for the full resolution and the AMR simulations. The depth of the boundary layer is simply defined as the altitude of the maximum azimuthal winds (ZMW), since it is generally observed that this height is coincident with the height where the radial inflow goes to zero. These statistics were computed

from $t=100$ to $t=200$ in the simulations. The mean C_v are within 1% of each other for the two cases and the mean A_V are with 2% of each other. The standard deviation of A_V is 12% less in the AMR simulation. The reason for this difference is not clear, although one can speculate that the larger numerical dissipation inherent to the regions of coarser gridding could decrease the variance in the AMR case. Nonetheless, these results are very encouraging because we are not interested in the exact evolution of axisymmetric tornado-like vortices, but rather in the long-time average maximum velocities and vortex structures generated by a particular set of model parameters (the strength of the convective forcing, the rotation rate, etc.).

The utility of adaptive mesh refinement is illustrated by considering the differences in memory use and CPU time between the full resolution and AMR cases. The full resolution simulation used $256 \times 128 = 32,768$ grid cells, and took 754 seconds of CPU time on a Sun Ultra 1 processor to integrate the equations of motion from $t=200$ to $t=201$. The AMR simulation with $Re_{cell} < 10$ at $t=200$ had a base grid of $64 \times 32 = 2048$ grid cells, one level 1 grid covering 56.25% of the domain with 4608 cells, and three level 2 grids covering 10.74% of the domain with 3520 cells, for a total of 10,176 cells. The CPU time on the same processor from $t=200$ to $t=201$ was 274 seconds.

4. Changes in Model Geometry

In this section we explore how changes in the size of the domain and the location and shape of the convective forcing field affect the structure and maximum windspeeds of the vortex. The names for each simulation and their relevant parameters are summarized in Table 1. The resulting velocity coefficients, vortex aspect ratios, and boundary layer depths for all the simulations are summarized in Table 2. Except where noted, these statistics were computed from $t=100$ to $t=200$ in each simulation.

a. Simulations with larger domains

Using a closed domain with a ceiling at $z=1$ certainly seems restrictive when using a convective forcing field that is maximized at $z=0.5$ and when the outflow from the vortex core clearly impinges on the ceiling, especially during the initial evolution of the vortex (see F93 and NF99). Our first step was to repeat the F93 simulation but with the upper boundary of the domain moved up to $z=2$, using AMR with a base grid of 64×64 gridpoints and an unlimited number of levels of refinement. This is simulation F93ZDBL. The time evolution of the maximum velocities and the vortex aspect ratio are shown in Fig. 7 and the azimuthal and vertical velocity fields are shown in Fig. 8. The vortex which ultimately develops in this simulation is essentially identical to the one which develops in the original F93 simulation. The notable difference in the results is that when the domain height is increased the vortex transitions much more rapidly to the unsteady dynamics observed in the last 100 time units of the F93 simulation, and it appears that the vortex is a bit more unsteady than before.

Another important observation is that the downward flow in the core of the vortex appears to be at least as vigorous as in the F93 simulation. This suggests that in the previous case the proximity of the ceiling did not enhance this downward flow. Simulations with still higher upper boundaries, and also outer boundaries that were further from the axis (not shown), gave equivalent results.

b. Convective forcing further from the surface

The way in which the evolution of the vortex depends on the altitude and the shape of the convective forcing field has previously been investigated by Trapp and Davies-Jones (1997). Using the same axisymmetric model as Fiedler (1994), with similar boundary conditions and convective forcing functions, they investigated under what circumstances the tornado-like vortex formed developed by a mechanism known as the *dynamic pipe effect* (DPE). A DPE occurs when

the lowest levels of the convective forcing are sufficiently far above the surface. At first, the convective forcing induces convergence of the rotating fluid only immediately below. The amount of actual fluid convergence which occurs is limited by the surrounding rotation, but the local intensification of the rotation creates a region of lower pressure beneath the convective forcing. This low pressure induces more convergence below, which then induces more low pressure and so on. By this mechanism the effect of convective forcing at high altitudes is propagated downwards until it reaches the surface, where due to interaction with the surface an intense vortex forms.

In this paper we focus not on the initial development of the vortex but on the long-term windspeeds and structure of the vortex which forms. Simulation HIBUBL was the same as F93ZDBL except that the height of the convective forcing was changed to $z_{forc} = 1.0$. The results are nearly identical to what we have seen before, except that the vortex is less unsteady and with a slightly lower aspect ratio. While the flow field near the surface is shown in Fig. 9 to be essentially the same as what we have seen before, we also see secondary maxima in the azimuthal and vertical velocities in the vicinity of $z=0.9$, $r=0.2$. These secondary maxima are caused by a local intensification of the rotation and vertical motion caused by the convective forcing field. Simulations with convective forcing at still higher altitudes (not shown) gave similar results.

c. The shape of the convective forcing

In the analysis of NF99, it was assumed that there was only one important length scale in the determination of the characteristics of the vortex. This length scale was assumed to be the vertical height of the domain, which also happened to be equal to the vertical and horizontal scales of the convective forcing. However, we have already shown that the size of the domain and the height of the convective forcing have little impact on the characteristics of the vortex.

It remains to be seen how the vertical and horizontal dimensions of the convective forcing

affect the results. For these simulations, the convective forcing remains centered at the altitude $z_{forc} = 1.0$. We proceed by first doubling the vertical extent of the convective forcing in a simulation called TALLBUBL. However, since the convective velocity scale U is determined by the integral of the forcing along the vertical axis, to keep $U=1$ we decrease the magnitude of the forcing by a factor of one half, i.e, $C_b = 0.632$. The results of such a simulation are summarized in Table 2 and we can see that there has been no appreciable change in the velocity coefficient or the aspect ratio.

Next, we return the vertical extent of the forcing to its original size and then double its horizontal extent for simulation WIDBUBL. Theoretically, this should not cause a change in the velocity scale. The resulting mean velocity coefficient of $C_v=0.7601$ is slightly higher, but clearly more significant are the changes in the mean and variance of A_V which are 3.8854 and 0.7808, respectively. It appears that increasing the horizontal extent of the convective forcing has substantially changed the structure of the vortex. The change can be seen in a snapshot of the azimuthal and vertical wind fields, shown in Fig. 10, where it is apparent that the vortex has a two-celled structure with a very wide core. What is the reason for this change? NF99 claimed that the structure should only depend on Re_V - but is in fact the structure also closely tied to the horizontal scale of the convective forcing?

Since the fluid in the far-field is in solid-body rotation, the circulation of the fluid increases with the square of the distance from the axis. If the convective circulation reaches out farther from the axis, the fluid it brings into the tornadic vortex will have a substantially higher circulation. Since the circulation of the fluid drawn into the vortex scales as $\Gamma \sim \Omega L^2$, we should be able to make a vortex with the same Re_V by reducing Ω to 25% of its previous value. To address this hypothesis we ran simulation WIDBUBL Ω 05 with the same convective forcing but with one

quarter the rotation rate, $\Omega=0.05$. The results, shown in Fig. 11 and Table 2, indicate that the vortex structure is once again that of a DVJ with an average $A_V=1.4085$. It also appears that wider convective forcing allows for slightly higher windspeeds. Further simulations with different convective forcing widths and rotation rates confirmed these observations. In regards to predicting the structure of the vortex, the appropriate length scale to use in the calculation of $Re_V = \Gamma/\nu = \Omega L^2/\nu$ is in fact the width of the convective forcing. This, however, only applies to simulations with solid-body rotation in the far-field.

Another interesting result is that the depth of the swirling boundary layer (ZMW) and the radius of maximum winds (RMW) are both approximately twice as large in simulation WID-BUBL Ω 05. The change in the depth of the boundary layer is surprising, since it did not increase in depth when the *only* change was to make the convective forcing wider. The relationship between the length scales in the vortex core and the horizontal scale of the convective forcing will be explored further in section 7.

5. Results for Higher Reynolds Numbers

Some of the most important claims made by NF99 were in regards to how the vortex behaves as the eddy viscosity ν is decreased. In particular, NF99 claimed that 1) as the viscosity is decreased, the circulation of the fluid must be decreased proportionally in order to keep the same vortex structure; 2) if one does decrease the circulation accordingly, the mean maximum windspeeds would increase; and 3) the maximum windspeeds were observed when the vortex was in a “low-swirl,” one-celled vortex structure. In the following sections we evaluate these claims using the AMR model.

a. Vortex structure

By substantially increasing the background rotation rate Ω , one can easily cause the struc-

ture of the vortex to change from a drowned vortex jump to that of a two-celled vortex. We call this simulation HISWIRL2CELL. An snapshot of the flow in this simulation is shown in Fig. 12ab, which is the result of an F93-type simulation with $\nu=0.0005$ (as before) and with $\Omega=0.5$. The vortex Reynolds number $Re_V=1000$ produces a vortex that jumps back and forth between two-celled and drowned vortex jump structures but spends most of its time in the two-celled state. These transitions are caused when large-amplitude axisymmetric rolls which are propagating down the vortex core reach the surface (see NF99). The vortex statistics are shown in Table 2.

Next we consider a similar simulation with $Re_V=1000$, but instead with $\nu=0.0002$ and $\Omega=0.2$, which is referred to as LOWSWIRL2CELL. This results again in a vortex with a predominantly two-celled structure, as shown in Fig. 12cd. The instantaneous flow structure is clearly more complicated in this case due to the substantially lower viscosity, but the overall structure of the vortex is quite similar to that in HISWIRL2CELL. The lower viscosity also allows for much higher mean windspeed with $C_v=0.8104$.

b. Maximum windspeeds

By decreasing Ω accordingly, we can recover the drowned vortex jump structure for the vortex when the model has lower viscosities, as in the previous section. The simulation LOWSWIRLDVJ refers to the case where $\Omega=0.08$ and $\nu=0.0002$. The drowned vortex structure is recovered (not shown) and we find $C_v=0.7972$. While this is noticeably higher than in all the F93-based simulations, it is smaller than that found above with the same viscosity and $\Omega=0.2$. In contrast to what was found by NF99, decreasing the rotation rate Ω so that the vortex evolved towards a “one-celled” structure does not in fact increase the maximum windspeeds. Rather, we find that the highest windspeeds are found with higher circulations that produce wide-based, two-celled vortices. Possible reasons for this difference will be discussed in the Conclusions.

We have endeavored to find the highest mean azimuthal windspeeds that our closed-domain model can produce. We have previously found that the windspeeds increase for smaller viscosities, and that the two-celled vortex structures have the highest windspeeds. We also saw above that the maximum windspeeds were somewhat higher for wider convective forcing fields. Despite the computational advantages offered by adaptive mesh refinement, the computational cost for equal amounts of simulation time increases drastically with increasing resolution - provided we maintain our refinement condition $Re_{Cell} < 10$. With these points in mind, we ran a simulation labelled LOWESTVISC which had $\Omega=0.05$, $\nu=0.0001$, and the wider convective forcing field with $\sigma_h=0.4472$. The resulting tornado-like vortex had substantially higher mean windspeeds than any of the previous simulations with a mean $C_p=0.9465$. The boundary layer was also slightly thinner and the vortex was more unsteady, as summarized by the results in Table 2. [Note: the statistics in this case were computed in a shorter time frame, from $t=40$ to $t=80$; with the much lower viscosity, the dynamics proceeded on a much shorter time scale, such that the vortex was well-developed and meaningful averages could be computed in this time interval.]

6. Tornado-Scale Simulations

a. Summary of important results

Let us summarize the important conclusions drawn from the previous two sections:

1. Increasing the size of the domain has little effect on the vortex structure and maximum windspeeds.
2. The altitude (height) and depth (vertical scale) of the convective forcing have little effect on low-level vortex structure and maximum windspeeds.
3. The width (horizontal scale) of the convective forcing determines the vortex structure to the extent to which it determines the circulation of the fluid that is drawn into the vortex core. Increasing the width also produces somewhat higher windspeeds, and seems to affect the depth of the boundary layer in

some cases.

4. Decreasing the viscosity allows for higher windspeeds and decreases the depth of the swirling boundary layer.

In the next section we will use these conclusions to attempt to produce tornado-like vortices on dimensional scales which match the characteristic scales of observed tornadoes.

b. Tornado-scale simulations

Observations, theory, and modelling all indicate that the necessary elements for a sustained tornado, and all tornado-like vortices (dust devils, waterspouts, etc.), is the interaction of sustained convection with an ample supply of rotating air near the surface. We now construct a simple model of such an occurrence. We again use a closed domain and a fixed convective vertical forcing field, but we re-write the magnitude of the forcing in terms of a maximum temperature anomaly T' and a mean background temperature \bar{T} in a Boussinesq fluid:

$$F_z = g \left(\frac{T'}{\bar{T}} \right) e^{-\left\{ \frac{r^2}{\sigma_h^2} + \frac{(z - z_{forc})^2}{\sigma_v^2} \right\}} \quad (6.1)$$

where g is the gravitational acceleration.

Rather than putting the system into solid body rotation, we instead construct a somewhat more realistic rotational environment. The azimuthal velocity field is initialized as a Rankine vortex with a maximum windspeed V^* which occurs at some radius of maximum winds r_{max} (not to be confused with RMW, the radius of maximum winds of the tornado-like vortex). However, unlike the solid-body rotation simulations, the azimuthal velocity is set to zero at the surface, and the transition between the no-slip surface and the Rankine vortex aloft is modelled with a logarithmic profile. Explicitly:

$$v_0(r, z) = \begin{cases} f(z)V^*r/r_{max} & r \leq r_{max} \\ f(z)V^*r_{max}/r & r > r_{max} \end{cases}, \quad (6.2)$$

with

$$f(z) = \begin{cases} 0 & z < z_0 \\ \frac{\log(z/z_0)}{\log(z_{top}/z_0)} & z_0 \leq z \leq z_{top} \\ 1 & z > z_{top} \end{cases} \quad (6.3)$$

where z_0 is the top of the friction layer and z_{top} is the top of the logarithmic layer. By setting v to zero below z_0 we are neglecting the azimuthal wind in the friction layer; alternatively we could consider z_0 to be a roughness length below which there is no meaningful flow.

We do not claim these initial conditions to be representative of any specific observations, rather they are a simple model of a large-scale circulation in contact with a no-slip surface. The fluid outside of r_{max} is intended to represent an unlimited supply of fluid with a constant circulation $2\pi V^*r_{max}$. To simulate this unlimited supply, we keep the circulation approximately constant in the far field (far from the tornado-like vortex) by adding a forcing term to the azimuthal momentum equation which continually drives the azimuthal velocity beyond r_{max} back to this constant value, i.e.,

$$F_\theta(r, z) = \begin{cases} 0 & r < r_{max} \\ -\tau^{-1}[v(r, z) - v_0(r, z)] & r \geq r_{max} \end{cases} \quad (6.4)$$

where τ is a time scale for the relaxation. The upper and lateral boundaries are also no-slip, but they are maintained at their initial rotation rate as defined by v_0 in (6.2).

The following tornado-scale simulations all share the following geometries: the dimen-

sional height and dimensional radius of the domain are both 4 km. The height of the convective forcing function $z_{forc}=2\text{km}$, with a width scale $\sigma_h=1.5\text{ km}$ and a vertical scale of $\sigma_v=1.0\text{ km}$. The maximum temperature anomaly $T' = 20\text{ K}$ and mean background temperature $\bar{T} = 280\text{ K}$. Assuming an air density of 1.0 kg m^{-3} , the CAPE associated with this convective forcing is 1235 J kg^{-1} , with the associated convective velocity scale $U=49.7\text{ m s}^{-1}$. The relaxation time for restoring the circulation of the fluid in the far-field is $\tau = 20\text{ sec}$. The base grid has a resolution of 256×256 gridpoints, so that the base grid spacing $\Delta r = \Delta z = 15.625\text{ m}$. We use the refinement criterion $Re_{cell} < 10$.

In the last few years the resolution of the observations of the wind field in tornadoes has increased greatly due to the availability and use of portable Doppler radars (Wurman et. al., 1996; Wurman, 1998; Gill and Wurman, 1998). Wurman, et al. (1996) observed a tornado with $V_{max} \approx 70\text{ ms}^{-1}$, $RMW \approx 100\text{ m}$, and $ZMW \approx 100\text{ m}$. We were able to produce tornado-like vortices with similar length scales from very reasonable values for the eddy viscosity ν and the far-field circulation Γ . As an example, we demonstrate the results of a simulation with $r_{max} = 2\text{km}$, $V^* = 4\text{ ms}^{-1}$, $z_0 = 3\text{ m}$, $z_{top} = 200\text{ m}$, and $\nu = 20\text{ m}^2\text{s}^{-1}$. The initial azimuthal velocity field and the convective forcing function are shown together in Fig. 13. The model vortex goes through a spin-up process similar to the solid-body rotation simulations, and then collapses into an intense, near-surface vortex.

Snapshots of the full azimuthal and vertical velocity fields at $t=1175\text{ s}$ are shown in Fig. 14. These results show a scale separation between the full model domain, the convective forcing, and intense, low-level vortex; note how small the intense vortex is in comparison with the large-scale features of the flow and the rest of the domain. A close-up of the azimuthal velocity field of the near-surface vortex is shown in Fig. 15, which in this case exhibits a drowned vortex jump

structure nearly identical in shape to many of the vortices generated in the solid-body rotation experiments. The RMW at this point is 99 m and the ZMW is 63 m, showing remarkable agreement with the observations of Wurman et al. (1996). The velocities are considerably lower, with $V_{max} = 39.8 \text{ ms}^{-1}$, as compared to the 70 ms^{-1} observed. This is due to our relatively weak convective forcing and the modest value of CAPE cited above. [Increasing the value of this CAPE would have required making the scale of the convective forcing closer to the size of the domain, or increasing the effective “temperature anomaly” to unrealistic values.] Nonetheless, we find that a tornado-like vortex very similar in structure to the one observed by Wurman et al. (1996) can be produced with a far-field circulation associated with a maximum azimuthal velocity of 4 ms^{-1} at 2 kms radius, and a constant eddy viscosity of $20 \text{ m}^2\text{s}^{-1}$.

These simulations are another excellent demonstration of the utility of adaptive mesh refinement. Note how the refinement occurs only regions of large shear, which occur near the boundaries and also in the vicinity of a few intense axisymmetric rolls. The majority of the domain, 73.9% is not refined; 26.1% of the domain is covered by level 1 refinement boxes with a grid spacing of 8.3 m, 4.45% of the domain is covered by level 2 refinement boxes with a grid spacing of 4.15 m, and just 1.05% of the domain is covered by level 3 refinement boxes with a grid spacing of 2.08 m. The total number of grid cells is 159186, whereas equivalent coverage with a constant-grid spacing model would take $2048^2 = 4194304$ grid cells.

The structure of these tornado-scale vortices can be manipulated by varying the viscosity and/or the far-field circulation in exactly the same manner as was shown above in the solid-body rotation simulations. For example, doubling the circulation in the far-field, by increasing the value of V^* in (6.2) from 4 ms^{-1} to 8 ms^{-1} , creates a tornado-scale vortex with a two-celled structure whose RMW is approximately doubled. A snapshot of this vortex is shown in Fig. 16a. On the

other hand, doubling the eddy viscosity to $\nu=40 \text{ m}^2\text{s}^{-1}$ changes the vortex structure from a DVJ to a one-celled vortex with lower mean windspeeds and a deeper boundary layer, as shown in Fig. 16b. Finally, increasing the width of the convective forcing function by 50%, by changing the value of σ_h to 2.25 kms, does not change the structure from that of a DVJ, as shown in Fig. 16c. However, as we saw above in simulation WIDBUBLQ05, ZMW and RMW have increased roughly in proportion to the change in σ_h as well. [To ensure non-interference of the outer boundary, this last simulation was performed with a domain that extended to 6000 m in the radial direction.]

7. Length Scales in Tornado-Like Vortices

What determines the length scales of the intense vortex? We observed that the depth of the boundary layer (ZMW) and the radius of maximum winds (RMW) show some dependence on the horizontal scale of the convective forcing. Furthermore, in solid-body rotation simulations, this horizontal scale determines the circulation of the fluid that is drawn into the vortex core. It therefore appears that the horizontal scale of the convective forcing, which we shall label L_h , is the best candidate for the fundamental length scale in the problem [i.e., it should be used for L in (1.1) and (1.3)]. We also have the convective velocity scale U , the far-field circulation Γ , and the eddy viscosity ν . NF99 showed that four different dimensionless parameters can be constructed from these four dimensional scales, and that any two (but only two) of them can be used together to describe the full range of possible outcomes. NF99 also found that the most useful choices of these four parameters to use together were the vortex Reynolds number Re_V and the convective Reynolds number Re_C , by showing that 1) the vortex structure depended almost exclusively on Re_V , and 2) for fixed Re_V , the maximum windspeeds increased with increasing Re_C . The small increase in maximum windspeeds seen with wider convective forcing also supports using L_h in the definition

of Re_C .

For the length scales in the vortex core, such as the depth of the swirling boundary layer, dimensional analysis suggests the following relationship:

$$ZMW = C_{ZMW} f(Re_C, Re_V) L_h = C_{ZMW} f\left(\frac{UL_h}{\nu}, \frac{\Gamma}{\nu}\right) L_h \quad (7.1)$$

where C_{ZMW} is an unknown coefficient, preferably of order one. A similar relationship should apply for RMW. Through a careful examination of our results, we can try to guess the nature of the function f . First, the results indicate that f is an only very weakly varying function of Re_C , possibly even constant for large values. This can be seen by comparing the results of simulations HISWIRL2CELL and LOWSWIRL2CELL. Between these two simulations, Re_V was held constant, but ν was decreased by 60%, requiring a large change in Re_C . Yet, the mean value of ZMW decreased only slightly. This suggests that to a first approximation we may neglect the variation of Re_C in f .

In simulation WIDBUBL, we doubled L_h , and yet the mean ZMW decreased slightly, rather than doubling in size. To resolve this discrepancy, recall that in the solid-body rotation simulations, the proper choice of circulation is $\Gamma = \Omega L_h^2$. Thus, changes in L_h alone will not cause a change in ZMW provided that the function $f(Re_V)$ has the form $f(Re_V) = Re_V^{-1/2}$. (The slight decrease in ZMW may be accounted for by a slight decrease in f with increasing $Re_C \propto L_h$, which we are neglecting.) This suggests the following simplified relationship for the depth of the boundary layer:

$$ZMW = C_{ZMW} \left(\frac{\nu}{\Gamma}\right)^{\frac{1}{2}} L_h \quad (7.2)$$

It is interesting to note that in the solid-body rotation case, (7.2) predicts $ZMW \sim (\nu/\Omega)^{1/2}$,

which is identical to the depth of the classic Ekman boundary layer (Greenspan, 1990, p. 36). If this relationship were accurate, then a single value of C_{ZMW} should be consistent with the results from all the simulations. Based on the observed mean values of ZMW, we computed the corresponding value of C_{ZMW} in all solid-body rotation simulations. The results are summarized in the last column of Table 2. Except for a single outlier resulting from the LOWESTVISC simulation, the computed values lie in entirely in the range $1.35 < C_{ZMW} < 1.51$, with a mean of 1.427. The outlier may be due to the substantially higher convective Reynolds number in this case, 4 times higher than in LOWSWIRL2CELL, or perhaps the vortex has not yet achieved a steady state after all.

Despite running the tornado-scale simulations out to more than 20 minutes of simulation time, none of the four vortices had reached a statistically steady state. Thus we could only estimate the mean depths of the swirling boundary layers in these cases. From these estimates, values of C_d were found ranging from 1.0 to 1.8. Nonetheless this indicates our theory also applies to the case when the circulation is constant in the far-field.

From the definition of the vortex aspect ratio A_V (1.6), we can also postulate the following approximate relationship for the radius of maximum winds,

$$RMW = A_V C_{ZMW} \left(\frac{v}{\Gamma} \right)^{\frac{1}{2}} L_h. \quad (7.3)$$

From NF99 and the results reported here, we know that the vortex aspect ratio is a monotonically increasing function of only the vortex Reynolds number, i.e., $A_V = A_V(Re_V)$. The nature of this function remains for future study.

8. Conclusions

Adaptive mesh refinement is a powerful tool which is likely to be used more frequently in the expanding field of computational fluid dynamics. This technique is particularly effective in domains with regular geometries, but where the flow is highly complex in a small fraction of the domain, such as when an intense, unsteady boundary layer develops. The near-surface dynamics of an intense, sustained vortex such as a tornado is an example of such a flow. In this report we have shown that the maximum windspeeds and vortex structure simulated with adaptive mesh refinement are nearly identical to those produced with a model with equivalent, constant grid spacing throughout the domain.

We have used adaptive mesh refinement to clarify and expand upon the previous results of Nolan and Farrell (1999a). The important conclusions are summarized in the beginning of section 6 above. The results indicate that the structure and maximum windspeeds of tornadoes are less dependent on the "details" of the storm environment than one might expect. In particular, the maximum windspeeds of tornadoes are almost solely dependent on the vertically integrated intensity of the overhead convection, with only a relatively weak dependence on the structure of the vortex (as indicated by the fact that the velocity coefficient lies in the relatively narrow range $0.7 < C_v < 1.0$). Furthermore, this intensity has only a weak dependence on the size and shape of the convection which sustains it. We do find that the highest windspeeds occur when the vortex has a two-celled structure with a wide base, which is in contrast with the earlier findings in NF99.

The reason for the difference between our results and those of NF99 likely has to do with numerical resolution in the boundary layer. As the vortex transitions to a two-celled state, the swirling boundary layer becomes progressively shallower. Under-resolution of this layer will lead to spurious dissipation of radial and angular momentum, ultimately causing lower mean wind-

speeds. While it has generally been reported in the literature that the highest windspeeds occur when the vortex is in the DVJ state (see the review by Church and Snow, 1993), some laboratory studies have found higher windspeeds in the high-swirl regime (Baker and Church, 1979). Fiedler (1994, 1998) also found the highest mean azimuthal windspeeds occurring in two-celled vortices. Certainly, this would be consistent with the general observation that most of the severest tornadoes have wide bases.

Our results did agree with the findings of NF99 that the structure of the vortex depends on the ratio of the circulation of the fluid that is drawn into the vortex to the eddy viscosity of the fluid, i.e., the vortex Reynolds number Γ/ν . Furthermore, by using dimensional scales for the convection and far-field circulation that are consistent with the tornado environment, we found that realistic values for the maximum windspeeds, the radius of maximum winds, and the depth of the tornadic boundary layer can be reproduced using typical values for the eddy viscosity such as $\nu=20 \text{ m}^2\text{s}^{-1}$; however, a minimum grid spacing of 2.08 meters was necessary to sufficiently resolve the dynamics. Since the effect of diffusion is by far the greatest in the near-surface boundary layer, the physical significance of the eddy viscosity carries over to the turbulence generated by surface roughness in actual tornadoes. This suggests that identical thunderstorm environments may produce very different tornadoes over different surfaces, i.e., land versus water, city buildings versus open plains. This is consistent with observations and laboratory experiments [see for example, the review by Church and Snow (1993) and the references therein.]

Certainly, asymmetric and three-dimensional processes are prevalent in tornadoes and will likely be critical in developing a complete understanding of these and other intense atmospheric vortices. Fiedler (1998) has shown that substantially higher transient, localized windspeed maxima are observed in three-dimensional models of tornado-like vortices. These instantaneous, high-

est windspeeds are associated with the smaller scale "suction vortices" that form in the region of large shear between the RMW and the relatively stagnant core. Furthermore, both numerical simulations (Lewellen et. al., 1997) and recent theoretical work on asymmetric vortex dynamics (Nolan and Farrell, 1999b) indicate that three-dimensional dynamics enhance the mean, azimuthally averaged windspeeds as well as the instantaneous maxima. Fortunately, continuing advances in computer speed and memory will allow for more three-dimensional modelling at higher and higher resolutions, along with higher-order turbulence closure schemes. It is also encouraging to note that the speed and memory savings associated with adaptive mesh refinement in two dimensions will be even more substantial in three dimensions.

For the purposes of this study, which required a large number of simulations integrated over long periods of time to acquire meaningful statistics, using an axisymmetric model was much more feasible. The use of an axisymmetric model by Trapp and Davies-Jones (1997) to study the dynamic pipe effect was similar in that it required a large number of simulations with varying parameters (see for example, their Table 1). Since further understanding of tornado-like vortex dynamics will likely require three-dimensional modelling, axisymmetric models may have reached the limit of their usefulness in this regard. Nonetheless, we have been able to show that some useful predictions can be made based only on the simplest features of the tornadic environment.

Acknowledgements

The authors would like to thank Profs. A. J. Chorin and G. I. Barenblatt for helpful discussions on dimensional analysis and fluid dynamics, and Dr. V. Larson for helpful comments on the manuscript. This work was supported in part by the Office of Science, Office of Advanced Computing Research, Mathematical, Information, and Computational Sciences Division, Applied Mathematical Sciences Subprogram, of the U. S. Department of Energy, under Contract No. DE-AC03-76SF00098. D. Nolan was also supported by the Office of Naval Research under contract N00014-93-1-0456 P0006.

References

- Almgren, A. S., J. B. Bell, P. Colella, L. H. Howell, and M. L. Welcome, 1998: A conservative adaptive projection method for the variable density incompressible Navier-Stokes equations. *J. Comp. Phys.*, **142**, 1-46.
- Almgren, A. S., J. B. Bell, and W. Y. Crutchfield, 1999: Approximate projection methods: Part I. Inviscid analysis. Submitted to *SIAM J. Sci. Comput.* Also available from the Lawrence Berkeley National Laboratory as report LBNL-43374.
- Almgren, A. S., J. B. Bell, and W. G. Szymczak, 1996: A numerical method for the incompressible Navier-Stokes equations based on an approximate projection. *SIAM J. Sci. Comput.*, **17**.
- Baker, G. L., and C. R. Church, 1979: Measurements of core radii and peak velocities in modelled atmospheric vortices. *J. Atmos. Sci.*, **36**, 2413-2424.
- Church, C. R., J. T. Snow, G. L. Baker, and E. M. Agee, 1979: Characteristics of tornado-like vortices as a function of swirl ratio: A laboratory investigation. *J. Atmos. Sci.*, **36**, 1755-1776.
- , 1993: Laboratory models of tornadoes. In *The Tornado: its structure, dynamics, prediction, and hazards*. C. Church, et. al., eds. American Geophysical Union, Washington, D. C.
- Fiedler, B. H., 1993: Numerical simulation of axisymmetric tornadogenesis in forced convection. In *The Tornado: its structure, dynamics, prediction, and hazards*. C. Church, et. al., eds. American Geophysical Union, Washington, D. C.

-----, 1994: The thermodynamic speed limit and its violation in axisymmetric numerical simulations of tornado-like vortices. *Atmosphere-Ocean*, **32**, 335-359.

-----, 1998: Wind-speed limits in numerically simulated tornadoes with suction vortices. *Q. J. R. Meteorol. Soc.*, **123**, 2377-2392.

Fiedler, B. H., and R. Rotunno, 1986: A theory for the maximum wind speeds in tornado-like vortices. *J. Atmos. Sci.*, **43**, 2328-2340.

Gill, S. S., and J. Wurman, 1998: Wind field evolution of the Dimmit, TX and Rolla, KS tornadoes. 19th Conference on Severe Local Storms, Amer. Met. Soc., Boston.

Greenspan, H. P., 1990: *The Theory of Rotating Fluids*. Breukelen Press, Brookline, 325 pp.

Howells, P. C., R. Rotunno, and R. K. Smith, 1988: A comparative study of atmospheric and laboratory analogue numerical tornado-vortex models. *Q. J. Roy. Met. Soc.*, **114**, 801-822.

Lewellen, W., D. Lewellen, and R. Sykes, 1997: Large-eddy simulation of a tornado's interaction with the surface. *J. Atmos. Sci.*, **54**, 581-605.

Lewellen, D. C., W. S. Lewellen, and J. Xia, 1998: The influence of a local swirl ratio on tornado intensification near the surface. Submitted to *J. Atmos. Sci.*

Nolan, D.S., and B. F. Farrell, 1999a: The structure and dynamics of tornado-like vortices. *J. Atmos. Sci.*, **56**, 2908-2936.

Nolan, D. S., and B. F. Farrell, 1999b: The intensification of two-dimensional swirling flows by stochastic, asymmetric forcing. *J. Atmos. Sci.*, **56**, in press.

Rotunno, R., 1977: Numerical simulation of a laboratory vortex. *J. Atmos. Sci.*, **34**, 1942-1956.

-----, 1979: A study in tornado-like vortex dynamics. *J. Atmos. Sci.*, **36**, 140-155.

Trapp, R. J., and R. Davies-Jones, 1997: Tornadogenesis with and without a dynamic pipe effect. *J. Atmos. Sci.*, **54**, 113-132.

Walko, R. L., and R. Gall, 1986: Some effects of momentum diffusion on axisymmetric vortices. *J. Atmos. Sci.*, **43**, 2137-2148.

Ward, N. B., 1972: The exploration of certain features of tornado dynamics using a laboratory model. *J. Atmos. Sci.*, **29**, 1194-1204.

Wurman, Joshua, 1998: Preliminary results from the ROTATE-98 tornado study. *19th Conference on Severe Local Storms*, Amer. Met. Soc., Boston.

Wurman, J., J. M. Straka, and E. N. Rasmussen, 1996: Fine-scale doppler radar observations of tornadoes. *Science*, **272**, 1774-1777.

List Of Tables

Table 1: Summary of all Simulation Parameters.

Table 2: Summary of statistical results for all simulations.

Figure Captions

- Figure 1: Contour plot of the mean value of the internal swirl ratio as a function of the domain rotation rate Ω and the eddy viscosity ν .
- Figure 2: Contour plot of the mean vortex aspect ratio as a function of the domain rotation rate and the eddy viscosity.
- Figure 3: Maximum vertical, azimuthal, and negative horizontal velocities for the F93 simulation with 256x128 gridpoints (solid), the AMR simulation with $Re_{cell} < 20$ (dash-dot), and the AMR simulation with $Re_{cell} < 10$ (dashed). The azimuthal velocities are defined by the curve with the highest values at $t=70$, the horizontal velocities are the lowest at $t=70$, and the vertical velocities are in between.
- Figure 4: Same as previous but for a) the maximum vertical velocities only, and b) for the maximum horizontal velocities only.
- Figure 5: A direct comparison velocity fields for the F93 simulations at $t=100.0$, a) azimuthal velocities, with AMR; b) vertical velocities, with AMR; c) azimuthal velocities with full resolution throughout the domain; d) vertical velocities with full resolution. Plots are restricted to the part of the domain where \cdot . Negative contours are dashed.
- Figure 6: Maximum velocities and vortex aspect ratios as a function of time during the AMR and full resolution F93 simulations: a) maximum velocities, AMR; b) vortex aspect ratio, AMR; c) maximum velocities, full resolution; d) vortex aspect ratio, full resolution.

Figure 7: Results for the F93DBL simulation: a) maximum velocities; b) vortex aspect ratio.

Figure 8: Azimuthal and vertical velocity fields at $t=200$ for the F93DBL simulation: a) azimuthal velocities; b) vertical velocities. Negative contours are dashed.

Figure 9: Azimuthal and vertical velocity fields at $t=200$ for the HIBUBL simulation: a) azimuthal velocities; b) vertical velocities. Negative contours are dashed.

Figure 10: Azimuthal and vertical velocities at $t=200$ for the WIDBUBL simulation: a) azimuthal velocities; b) vertical velocities. Negative contours are dashed.

Figure 11: Azimuthal and vertical velocities at $t=200$ for the WIDBUBL $\Omega.05$ simulation: a) azimuthal velocities; b) vertical velocities. Negative contours are dashed.

Figure 12: Azimuthal and vertical velocities at $t=200$ for the HISWIRL2CELL and LOWSWIRL2CELL simulations and : a) azimuthal velocities, HISWIRL2CELL; b) vertical velocities, HISWIRL2CELL; c) azimuthal velocities, LOWSWIRL2CELL, d) vertical velocities, LOWSWIRL2CELL. Negative contours are dashed.

Figure 13: Contour plots of the initial azimuthal velocity field (solid) and the effective temperature anomaly associated with the convective forcing for the tornado-scale simulations.

Figure 14: Contour plots of the a) azimuthal and b) vertical velocity fields for the full domain at $t=1175$ sec in a tornado-scale simulation. Negative contours are dashed.

Figure 15: Close-up of the azimuthal velocity field in the low-level vortex generated in the tornado-scale simulation at $t=1175$ sec.

Figure 16: Examples of the azimuthal wind fields for three variations on the tornad-scale simulations: a) with twice the circulation; b) with twice the eddy viscosity; and c) with a convective forcing function 50% wider.

Table 1 Summary of all Simulation Parameters.

Simulation Name	Domain Height	Base Grid	Max. ref. lvs.	Ω	ν	z_{forc}	σ_h	σ_v
F93FULL	1.0	256x128	0	0.2	0.0005	0.5	0.2236	0.2236
F93AMR	1.0	64x32	2	0.2	0.0005	0.5	0.2236	0.2236
F93ZDBL	2.0	64x64	3	0.2	0.0005	0.5	0.2236	0.2236
HIBUBL	2.0	64x64	3	0.2	0.0005	1.0	0.2236	0.2236
TALL-BUBL	2.0	64x64	3	0.2	0.0005	1.0	0.2236	0.4472
WIDBUBL	2.0	64x64	3	0.2	0.0005	1.0	0.4472	0.2236
WID-BUBL Ω 05	2.0	64x64	3	0.05	0.0005	1.0	0.4472	0.2236
HISWIRL 2CELL	1.0	128x64	3	0.5	0.0005	0.5	0.2236	0.2236
LOW SWIRL 2CELL	1.0	128x64	3	0.2	0.0002	0.5	0.2236	0.2236
LOW SWIRL DVJ	1.0	128x64	3	0.08	0.0002	0.5	0.2236	0.2236
LOWEST VISC	1.0	256x128	3	0.05	0.0001	0.5	0.4472	0.2236

Table 2 Summary of statistical results for all simulations.

Simulation	\bar{C}_v	\overline{ZMW}	\bar{A}_V	$\left(\overline{(A_V - \bar{A}_V)^2}\right)^{\frac{1}{2}}$	C_{ZMW}
F93FULL	0.7318	0.0725	1.7400	0.4810	1.450
F93AMR	0.7320	0.0722	1.7509	0.4262	1.444
F93ZDBL	0.7444	0.0726	1.6188	0.5677	1.452
HIBUBL	0.7384	0.0683	1.7039	0.2517	1.366
TALL BUBL	0.7360	0.0717	1.5891	0.2732	1.434
WIDBUBL	0.7609	0.0716	3.8854	0.7808	1.432
WID BUBL Ω 05	0.7838	0.1370	1.4085	0.4797	1.370
HISWIRL 2CELL	0.7067	0.0475	2.9733	0.3941	1.502
LOW SWIRL 2CELL	0.8129	0.0454	2.7966	0.8140	1.436
LOW SWIRL DVJ	0.7970	0.0694	1.4864	0.3521	1.388
LOWEST VISC	0.9465	0.0394	1.9725	0.8838	0.881

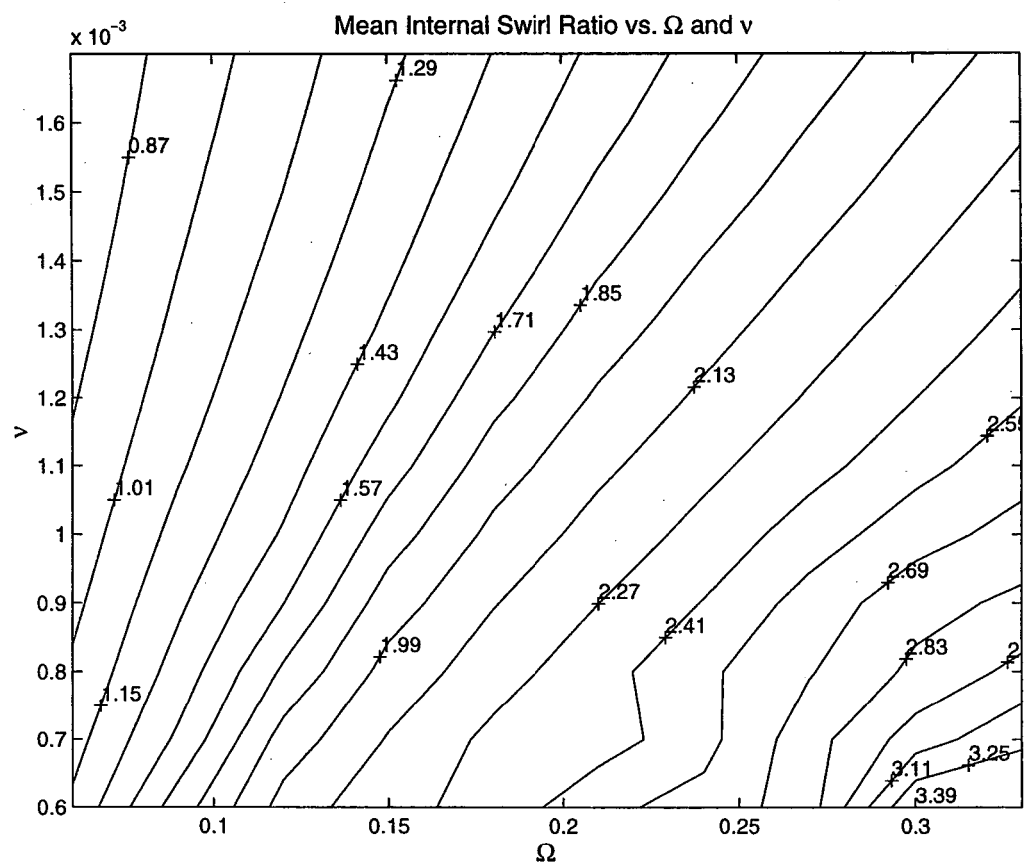


Fig. 1 Contour plot of the mean value of the internal swirl ratio as a function of the domain rotation rate Ω and the eddy viscosity ν .

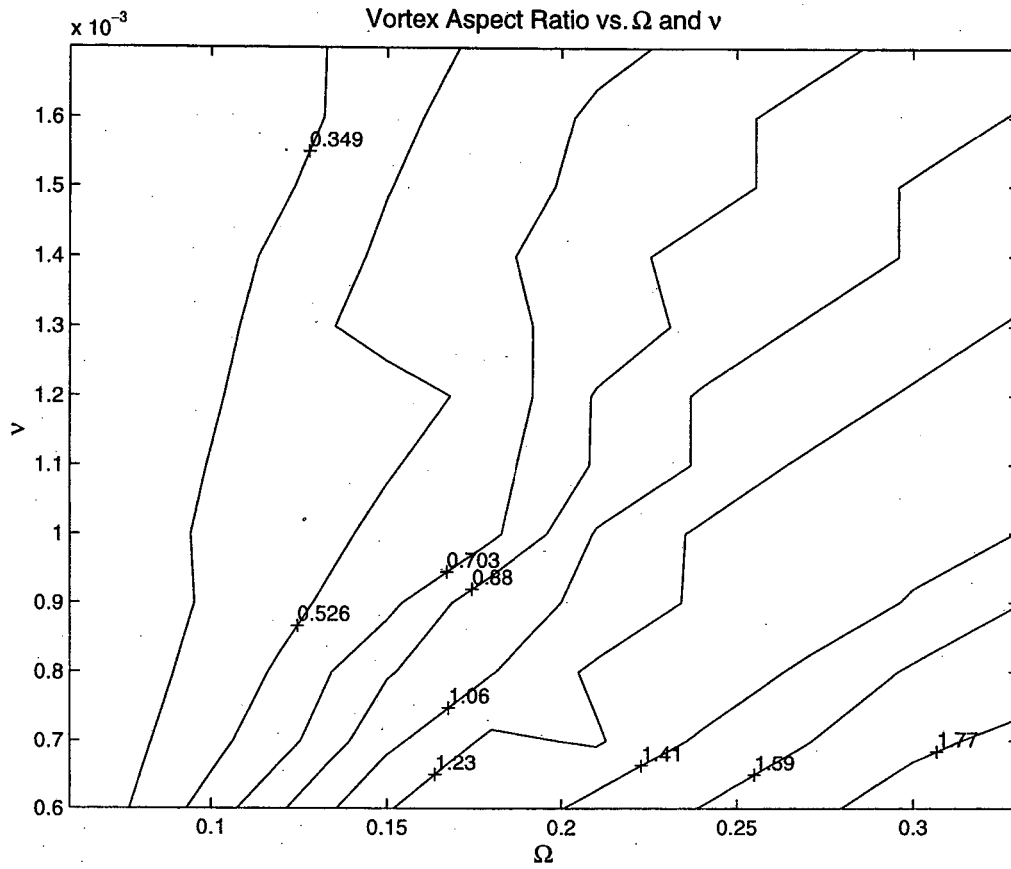


Fig. 2 Contour plot of the mean vortex aspect ratio as a function of the domain rotation rate and the eddy viscosity.

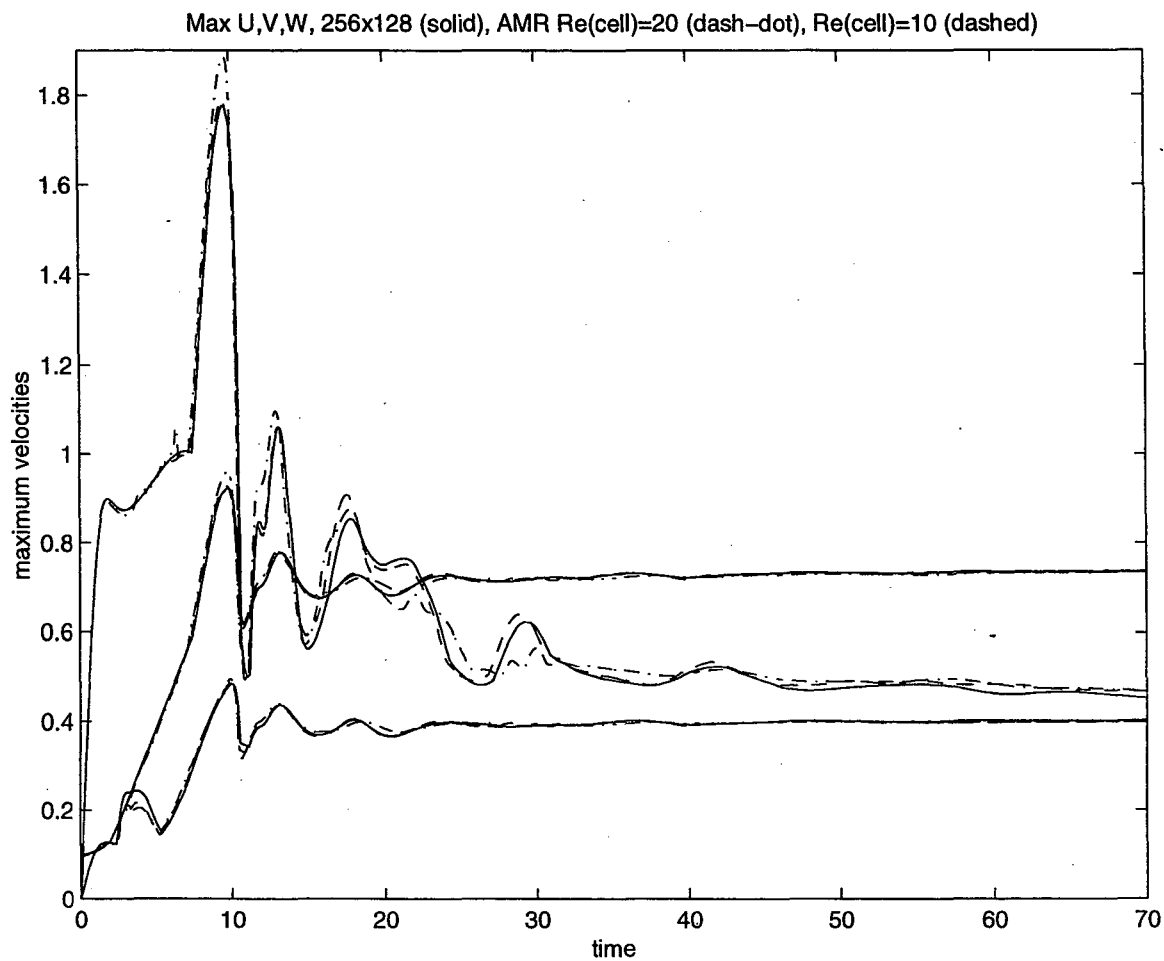


Fig. 3 Maximum vertical, azimuthal, and negative horizontal velocities for the F93 simulation with 256x128 gridpoints (solid), the AMR simulation with $Re_{cell}<20$ (dash-dot), and the AMR simulation with $Re_{cell}<10$ (dashed). The azimuthal velocities are defined by the curve with the highest values at $t=70$, the horizontal velocities are the lowest at $t=70$, and the vertical velocities are in between.

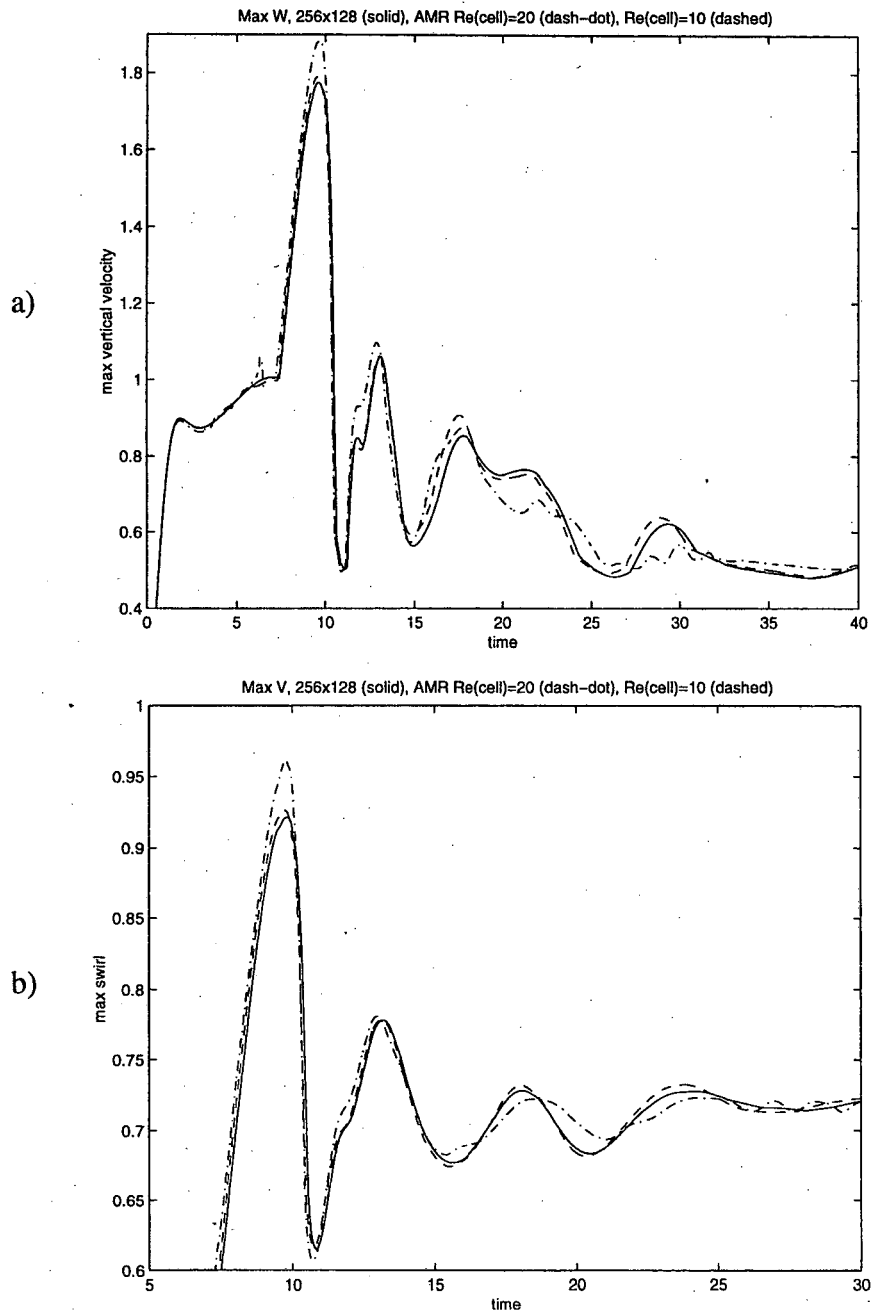


Fig. 4 Same as previous but for a) the maximum vertical velocities only, and b) for the maximum horizontal velocities only.

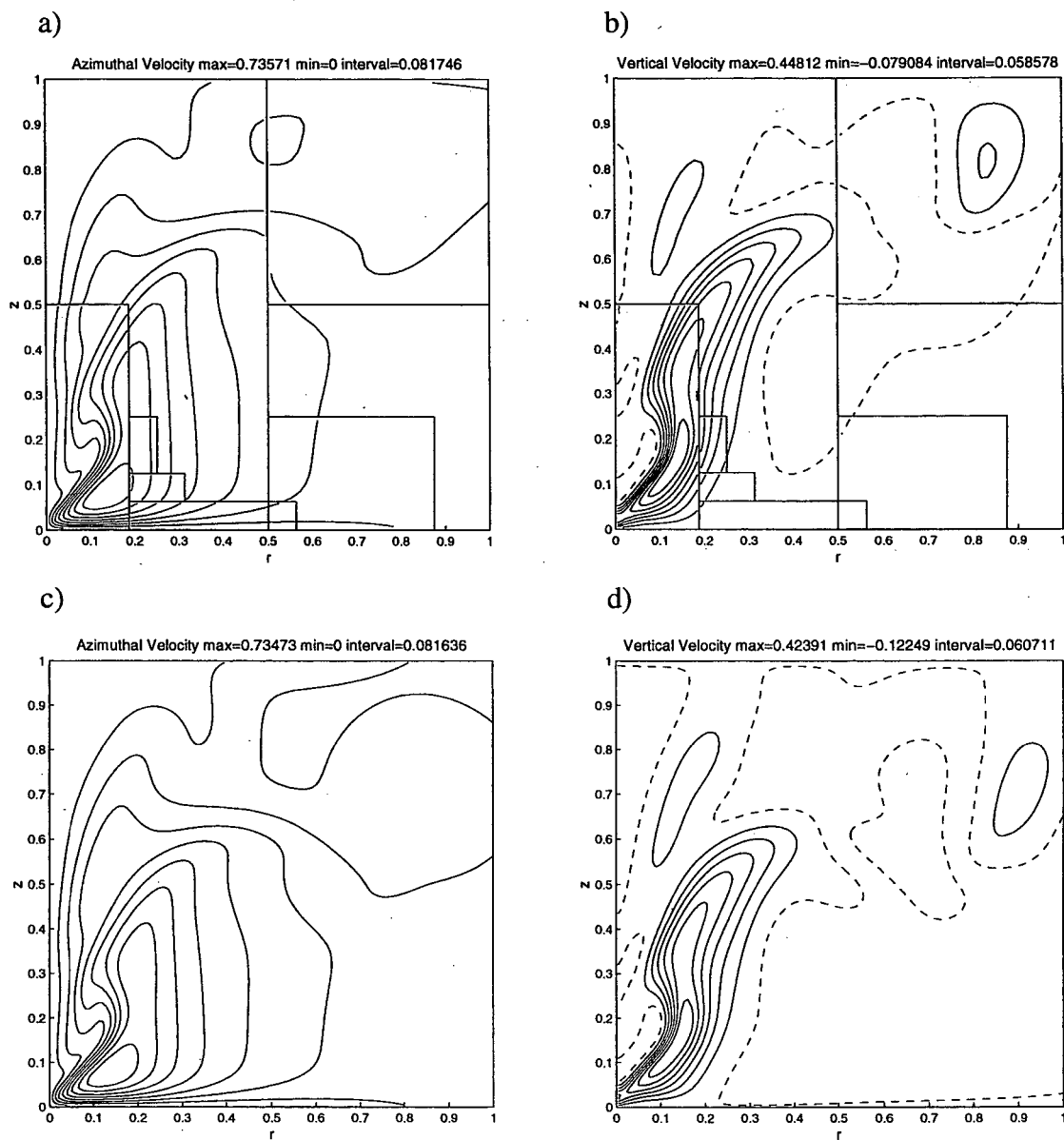


Fig. 5 A direct comparison velocity fields for the F93 simulations at $t=100.0$, a) azimuthal velocities, with AMR; b) vertical velocities, with AMR; c) azimuthal velocities with full resolution throughout the domain; d) vertical velocities with full resolution. Plots are restricted to the part of the domain where $0 \leq r \leq 1$. Negative contours are dashed.

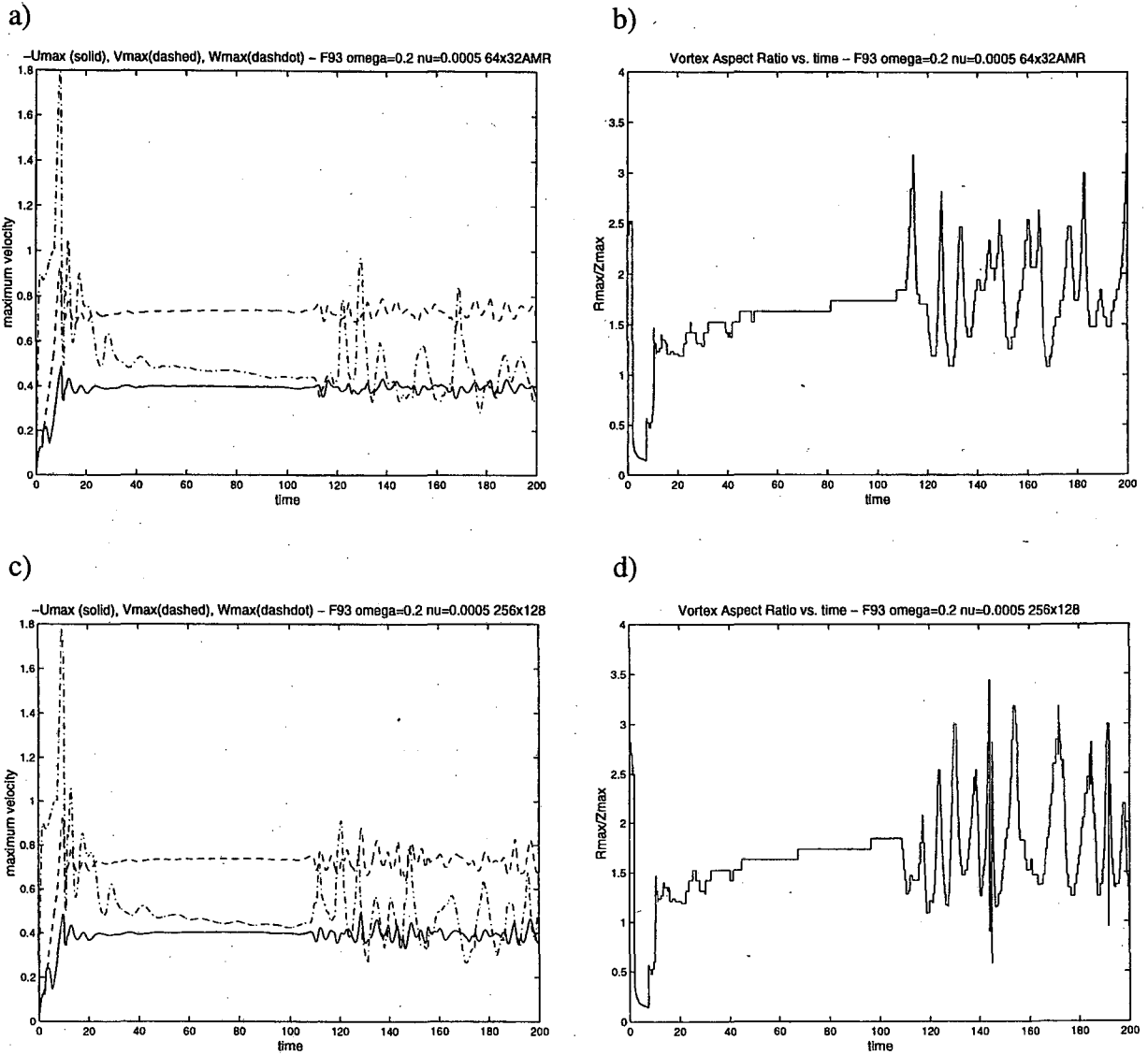


Fig. 6 Maximum velocities and vortex aspect ratios as a function of time during the AMR and full resolution F93 simulations: a) maximum velocities, AMR; b) vortex aspect ratio, AMR; c) maximum velocities, full resolution; d) vortex aspect ratio, full resolution.

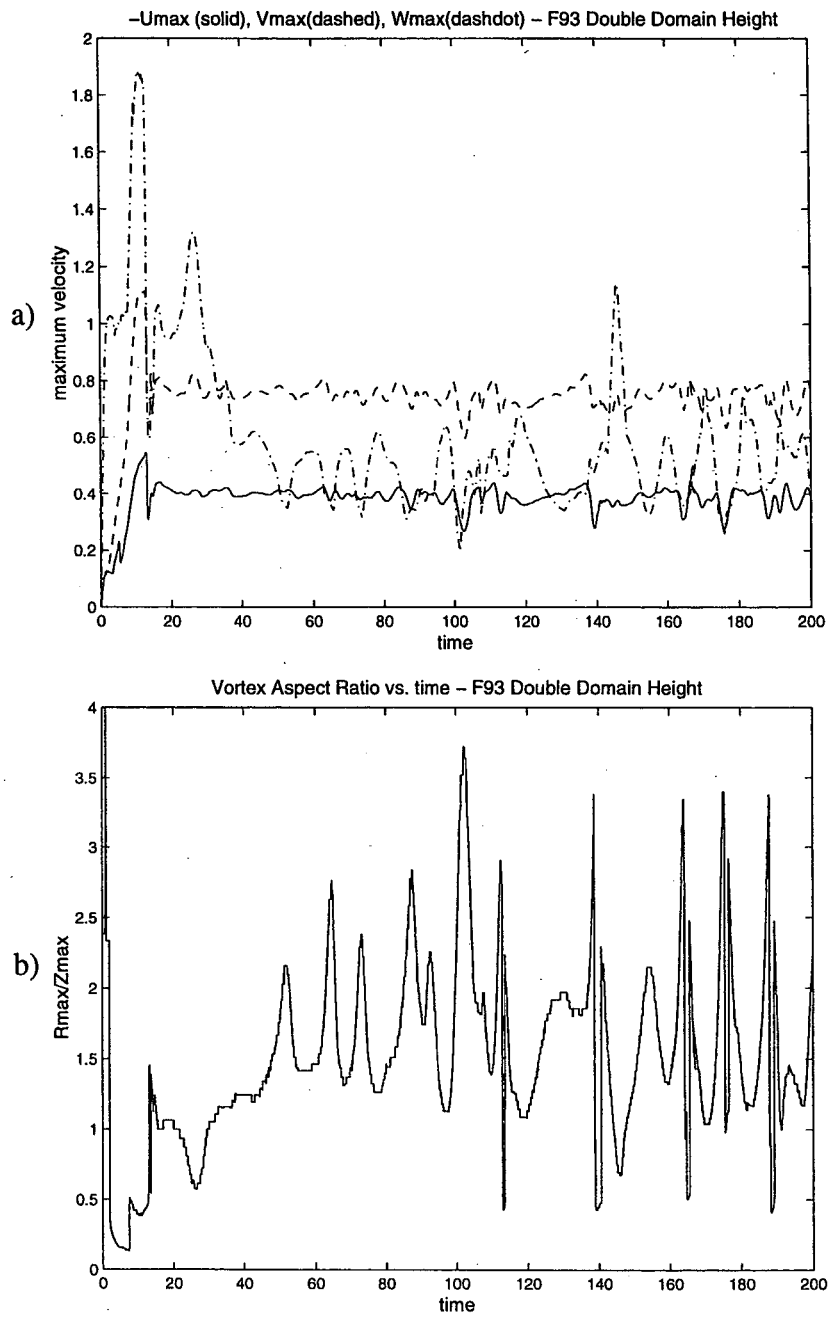


Fig. 7 Results for the F93DBL simulation: a) maximum velocities; b) vortex aspect ratio.

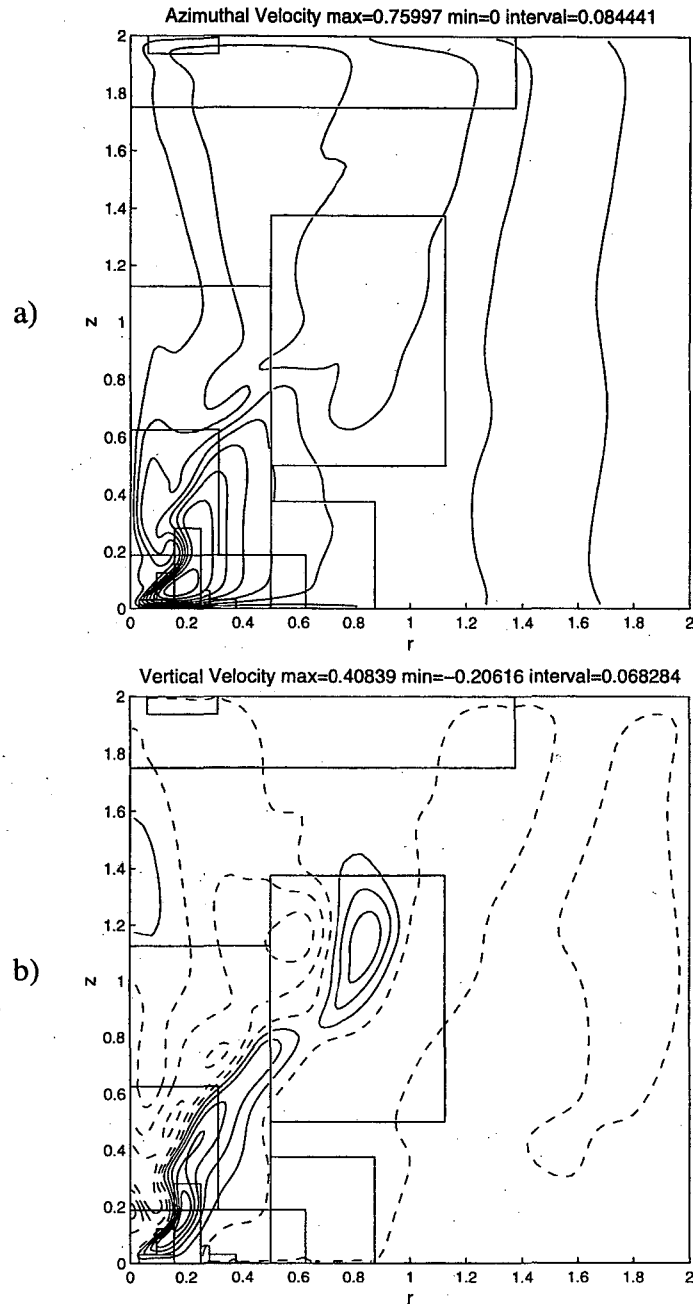


Fig. 8 Azimuthal and vertical velocity fields at $t=200$ for the F93DBL simulation: a) azimuthal velocities; b) vertical velocities. Negative contours are dashed.

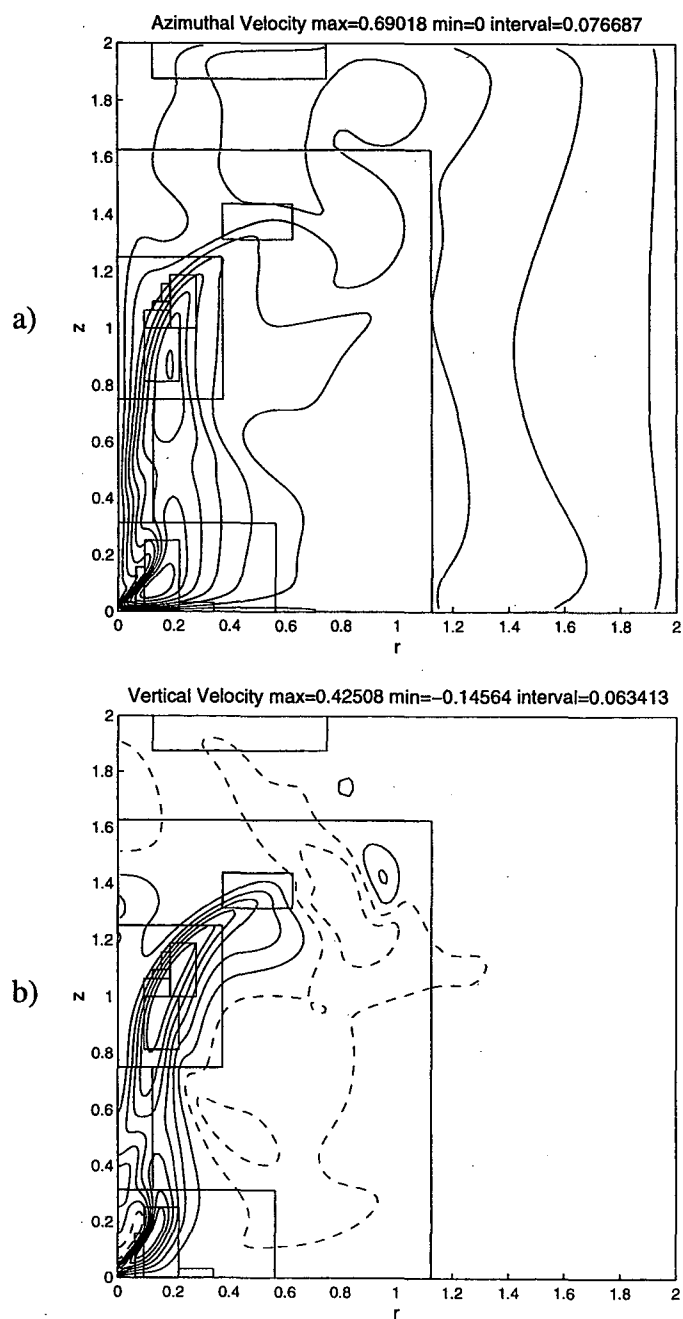


Fig. 9 Azimuthal and vertical velocity fields at $t=200$ for the HIBUBL simulation: a) azimuthal velocities; b) vertical velocities. Negative contours are dashed.

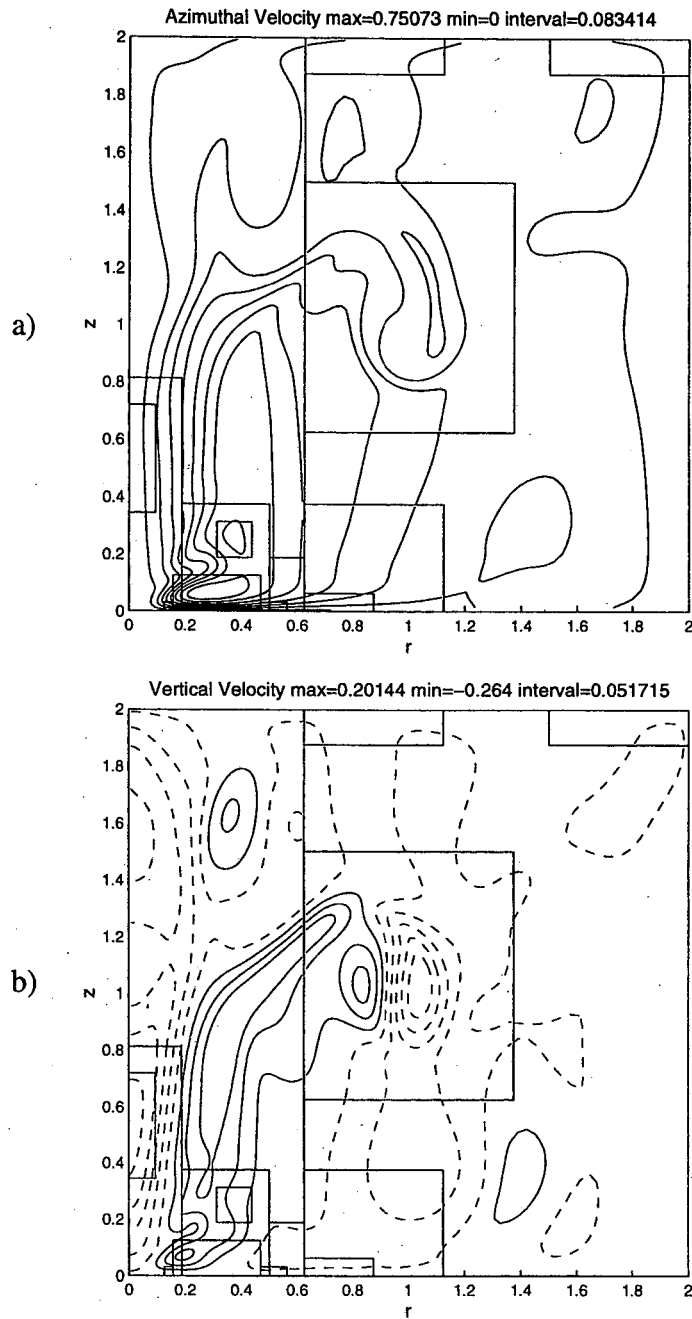


Fig. 10 Azimuthal and vertical velocities at $t=200$ for the WIDBUBL simulation: a) azimuthal velocities; b) vertical velocities. Negative contours are dashed.

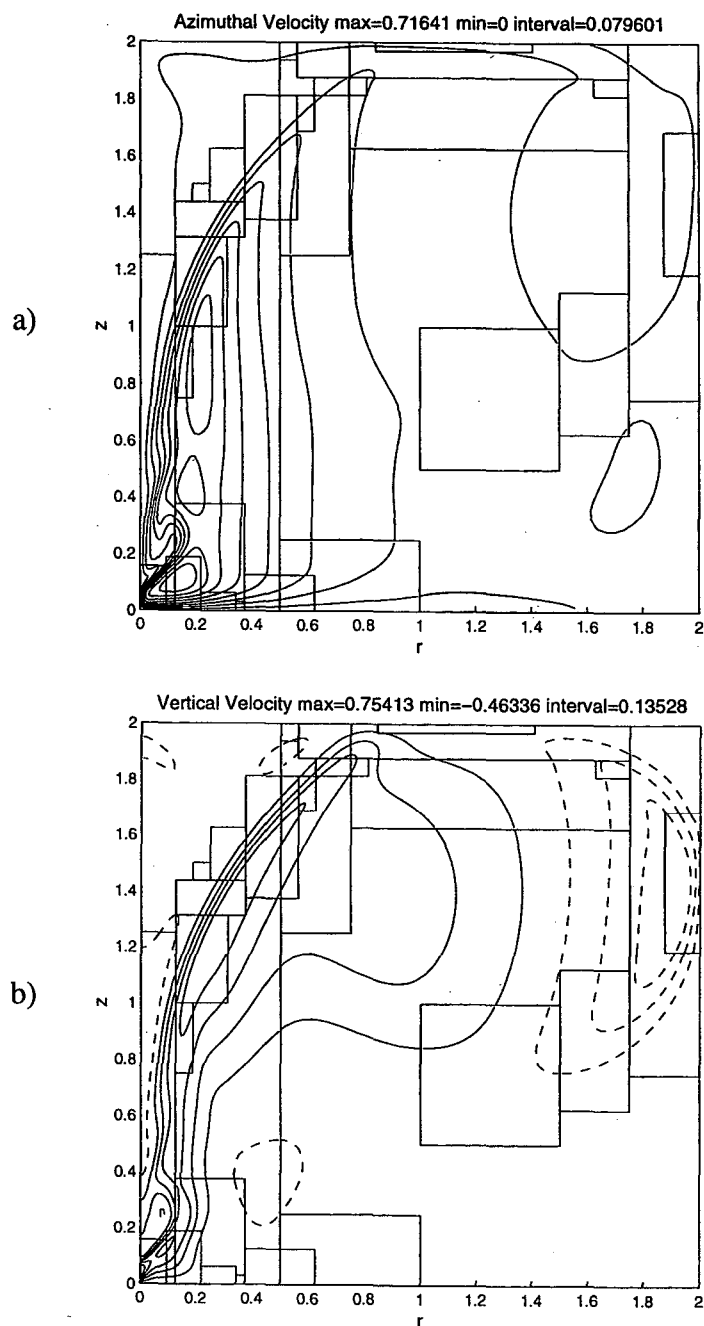


Fig. 11 Azimuthal and vertical velocities at $t=200$ for the WIDBUBL Ω 05 simulation: a) azimuthal velocities; b) vertical velocities. Negative contours are dashed.

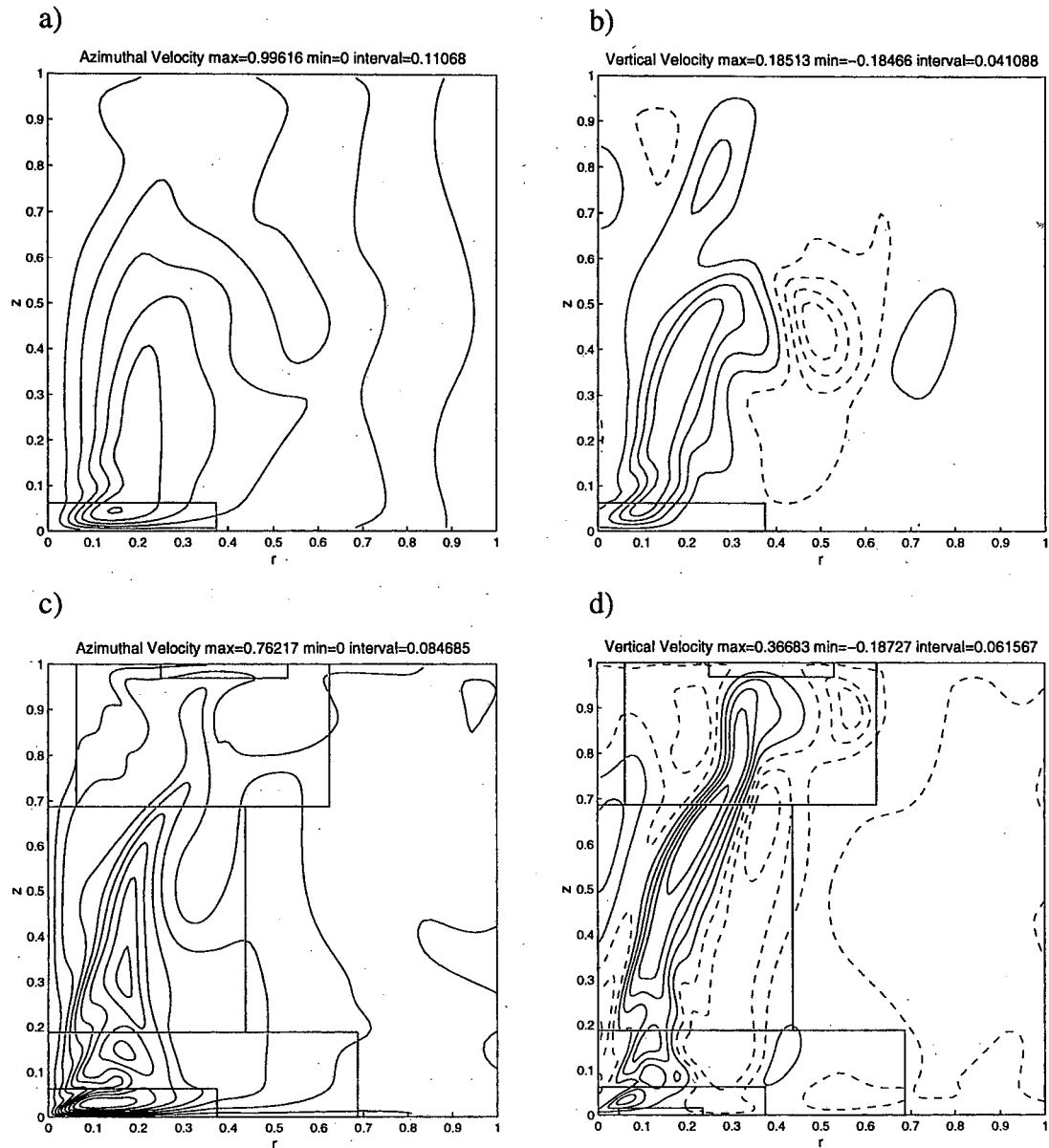


Fig. 12 Azimuthal and vertical velocities at $t=200$ for the HISWIRL2CELL and LOWSWIRL2CELL simulations and : a) azimuthal velocities, HISWIRL2CELL; b) vertical velocities, HISWIRL2CELL; c) azimuthal velocities, LOWSWIRL2CELL, d) vertical velocities, LOWSWIRL2CELL. Negative contours are dashed.

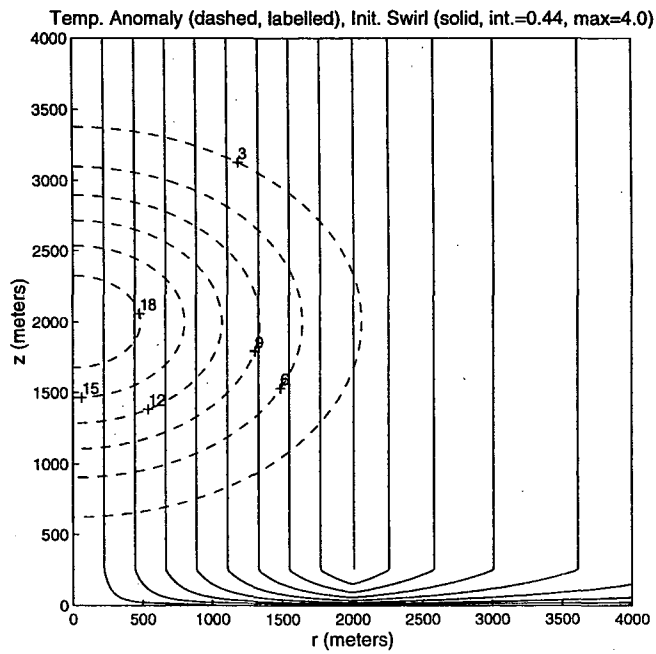


Fig. 13 Contour plots of the initial azimuthal velocity field (solid) and the effective temperature anomaly associated with the convective forcing for the tornado-scale simulations.

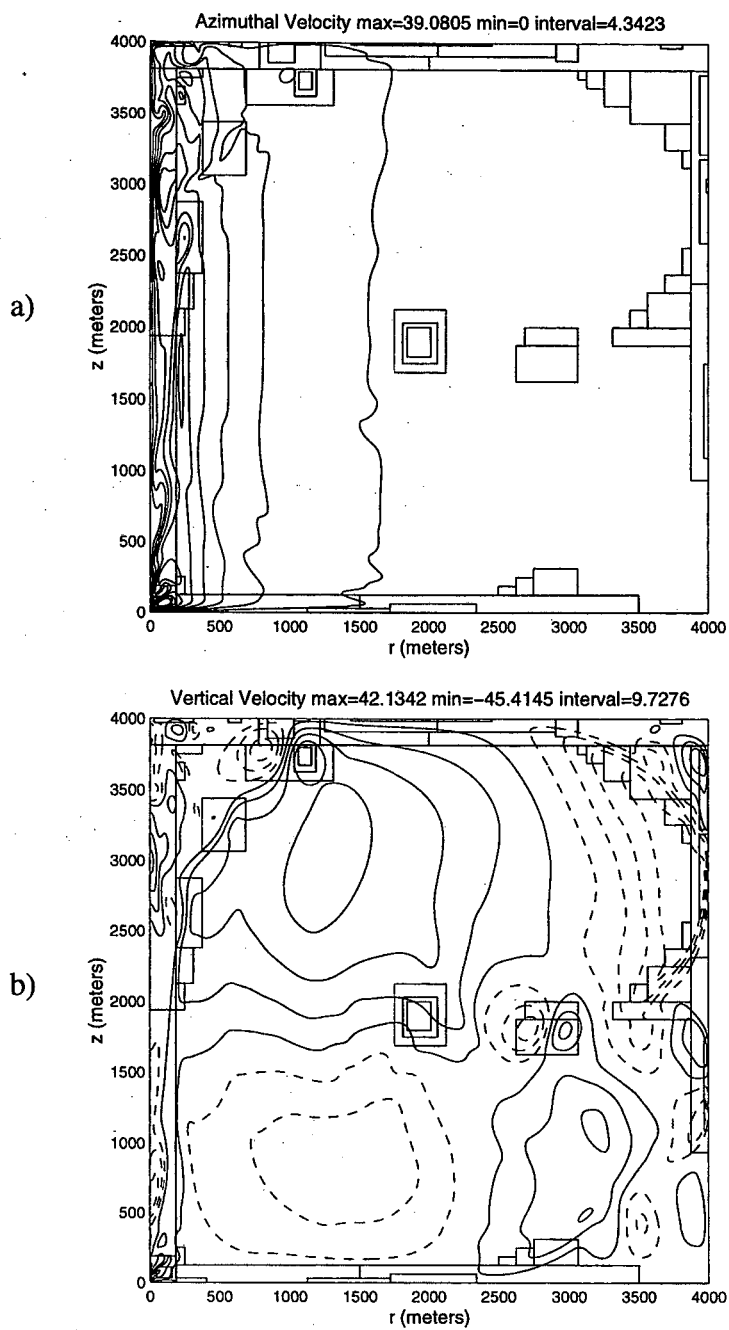


Fig. 14 Contour plots of the a) azimuthal and b) vertical velocity fields for the full domain at $t=1175$ sec in a tornado-scale simulation. Negative contours are dashed.

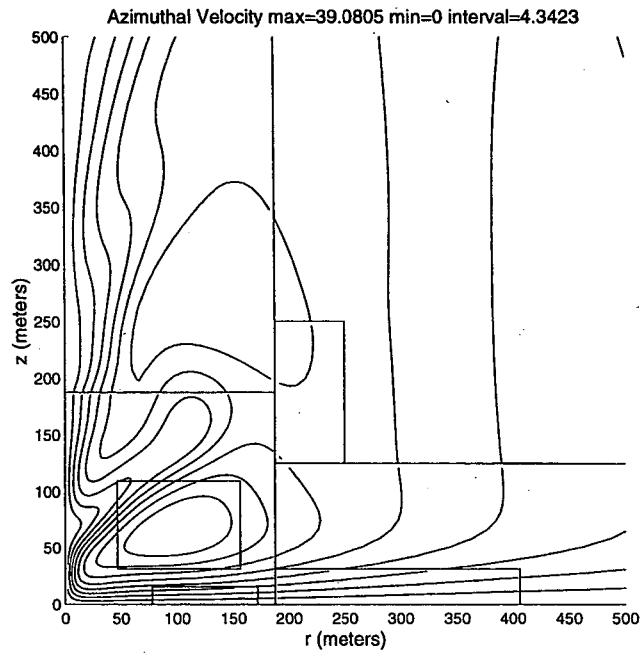


Fig. 15 Close-up of the azimuthal velocity field in the low-level vortex generated in the tornado-scale simulation at $t=1175$ sec.

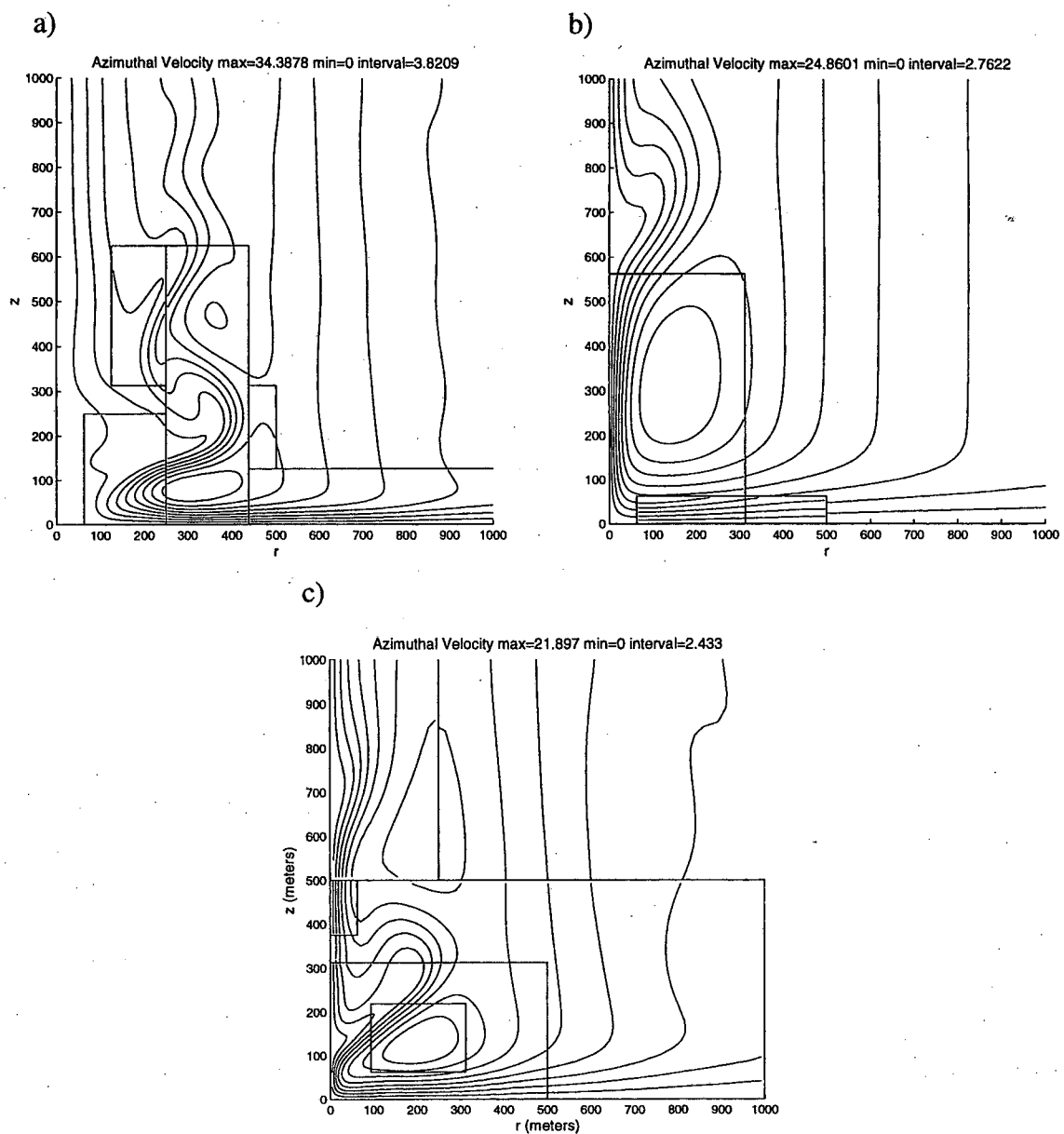


Fig. 16 Examples of the azimuthal wind fields for three variations on the tornad-scale simulations: a) with twice the circulation; b) with twice the eddy viscosity; and c) with a convective forcing function 50% wider.

**ERNEST ORLANDO LAWRENCE BERKELEY NATIONAL LABORATORY
ONE CYCLOTRON ROAD | BERKELEY, CALIFORNIA 94720**